Long-term climate impacts of large stratospheric water vapor perturbations

Martin Jucker,[a] Chris Lucas,[b] and Deepashree Dutta [a]

[a] *Climate Change Research Centre and Centre of Excellence for Climate Extremes, University of New South Wales, Sydney, Australia*
[b] *Bureau of Meteorology, Melbourne, Australia*

ABSTRACT: The amount of water vapor injected into the stratosphere after the eruption of Hunga Tonga-Hunga Ha'apai (HTHH) was unprecedented, and it is therefore unclear what it might mean for surface climate. We use chemistry climate model simulations to assess the long-term surface impacts of stratospheric water vapor (SWV) anomalies similar to those caused by HTHH, but neglect the relatively minor aerosol loading from the eruption. The simulations show that the SWV anomalies lead to strong and persistent warming of Northern Hemisphere landmasses in boreal winter, and austral winter cooling over Australia, years after eruption, demonstrating that large SWV forcing can have surface impacts on a decadal timescale. We also emphasize that the surface response to SWV anomalies is more complex than simple warming due to greenhouse forcing and is influenced by factors such as regional circulation patterns and cloud feedbacks. Further research is needed to fully understand the multi-year effects of SWV anomalies and their relationship with climate phenomena like El Niño Southern Oscillation.

SIGNIFICANCE STATEMENT: Volcanic eruptions typically cool the Earth's surface by releasing sulfur dioxide, which then converts into aerosols which reflect sunlight. However, a recent eruption released a significant amount of water vapor — a strong greenhouse gas — into the stratosphere with unknown consequences. This study neglects the aerosol effect and examines the consequences of large stratospheric water vapor anomalies and reveals that surface temperatures across large regions of the world increase by over 1.5°C for several years, although some areas experience cooling close to 1°C. Additionally, the research suggests a potential connection between the eruption and sea surface temperatures in the tropical Pacific, which warrants further investigation.

1. Introduction

Large volcanic eruptions can have significant and long-lasting impacts on climate (Robock 2000), as demonstrated by the El Chichón and Mt Pinatubo eruptions in the 1980s and 1990s, respectively. These eruptions released massive amounts of sulfur dioxide into the atmosphere, leading to the formation of stratospheric sulfate aerosol and global cooling of around 0.5-1.0 K. While the focus has largely been on these larger eruptions, recent studies suggest that even smaller volcanic events can have a measurable impact on climate (Vernier et al. 2011; Santer et al. 2014).

On 15 January 2022, the submarine volcano Hunga Tonga-Hunga Ha'apai (HTHH) erupted in the Southern Hemisphere (SH) subtropical Pacific Ocean with unprecedented intensity, producing eruption plumes that reached altitudes of 58 km in the upper stratosphere and lower mesosphere (Carr et al. 2022; Proud et al. 2022). Besides releasing only 0.4-0.5 Tg of sulfur dioxide (Carn et al. 2022; Gupta et al. 2022), which is lower than high climate impact events noted earlier, the eruption injected a large amount of water vapor into the stratosphere, equivalent to 5-10% of the climatological amount (Vömel et al. 2022; Millán et al. 2022). This stratospheric water vapor (SWV) can have both cooling and warming effects on the climate, and the potential impacts of the HTHH SWV release on the climate are still largely unknown. Recent studies of HTHH have shown that radiative forcing from SWV should be expected to dominate over aerosol forcing after a few weeks (Schoeberl et al. 2023a; Sellitto et al. 2022).

Enhanced SWV can contribute to surface warming (Dessler et al. 2013) and changes to the tropospheric and stratospheric circulation patterns (Maycock et al. 2013). It can also influence the formation of polar stratospheric clouds (PSCs), and lead to increased hydroxyl radical concentrations, which both play a key role in stratospheric ozone depletion (Solomon 1999; Tritscher et al. 2021). The impacts of the HTHH SWV release on PSC formation and ozone chemistry are uncertain and should be expected to depend not only on chemical, but also dynamical evolution of the initial cloud.

Once it reaches the stratosphere, SWV is transported in the zonal direction by the prevailing stratospheric winds, and in the vertical and meridional direction by the stratospheric overturning circulation, the so-called Brewer-Dobson circulation (BDC, Brewer 1949; Dobson 1956; Plumb 2002). As a result, the initially strongly confined plume becomes a widely distributed SWV anomaly in the zonal direction, but the meridional and vertical evolution is much slower. In the zonal mean picture, SWV is advected by the BDC on seasonal to multi-year timescales, but its distribution in the stratosphere is also constrained by the

Corresponding author: Martin Jucker, publications@martinjucker.com

Deepashree Dutta's current affiliation: Cambridge University, U.K.

strength of zonal winds, such as the polar vortex or the phase of the tropical Quasi-Biennial Oscillation (Holton and Tan 1980; Baldwin et al. 2001), which can act as transport barriers.

This work examines the impact of an SWV disturbance resembling that of the HTHH eruption and focus on the long-term effect of SWV on surface climate, while neglecting the effects of aerosol loading, which have been described elsewhere (e.g., Millán et al. 2022; Sellitto et al. 2022; Schoeberl et al. 2023a; Manney et al. 2023). This choice is motivated by the much longer residence times of SWV as compared to aerosols, meaning that aerosol contributions to climate anomalies on a multi-year timescale after eruption can be expected to be negligible compared to those of SWV (Sellitto et al. 2022; Schoeberl et al. 2023a; Guzewich et al. 2022). We will show that while the global mean temperature anomalies are expected to be small, regional impacts can be large, and, most importantly, long-lasting. After introducing the data and models we use for this study, we will examine the stratospheric evolution of the water vapor cloud and ozone concentrations in Section 3. Section 4 will describe the long-term surface impacts, before analyzing the mechanisms behind those impacts in Section 5, and concluding the paper in Section 6.

2. Data and model setup

We utilize data collected by NASA's Aura Microwave Limb Sounder (MLS) instrument (Waters et al. 2006) to analyze the HTHH cloud's initial characteristics and evolution, and employ version 4 of the Whole Atmosphere Community Climate Model (WACCM4) to address our research questions. Our research focus is not on recreating the HTHH eruption in every detail. Instead, we investigate the long-term climate effects of a spontaneous and locally bounded perturbation in stratospheric water vapor based on the scale and shape of the perturbation caused by the HTHH eruption.

a. Initial water vapour perturbation

The details of data retrieval and processing for MLS satellite data are given in Supplementary SA, and we content ourselves with summarizing the main results required for setting up our model simulations.

We estimate the vertical profile and approximate shape of the SWV anomaly in the initial states from three overpasses from 16 January 2022, and compare SWV values to those obtained from a 2005-2021 climatology. Our best estimate from these data is an anomaly of about 100 Tg of SWV, with a shape illustrated in Fig. 1.

Our estimate is between the 50 Tg derived from radiosonde data (Vömel et al. 2022) and the 146 ± 5 Tg from Millán et al. (2022), who utilized version 4 of the MLS data. The key divergence between our estimate and that of Millán et al. is that we identify a 47 Tg SWV anomaly that is present before the 15 January 2022 eruption, and is therefore not included in our estimates of the perturbation associated with this specific eruption (Figs. S2, S3).

b. Model simulations

1) WACCM

We conduct our numerical experiments using the Whole Atmosphere Community Climate Model version 4 (WACCM4)(Marsh et al. 2013). WACCM4 is a high-top, fully interactive chemistry-climate model with a 1.875 × 2.5° finite volume grid and 66 hybrid sigma levels extending from the surface to the lower thermosphere (140 km). WACCM4 includes all the physical parameterizations of the Community Atmosphere Model, Version 4 (Hurrell et al. 2013) and is coupled to the Community Land Model Version 4 (CAM4, Oleson et al. 2010) without dynamic vegetation or an active carbon-nitrogen cycle. CAM4 has been tested extensively and found to perform well with respect to tropospheric circulation and cloud processes (Neale et al. 2013). The fully interactive chemistry module in WACCM4 is based on the Model for Ozone and Related Chemical Tracers (MOZART) version 3 (Kinnison et al. 2007). The stratospheric temperature, chemical and radiative processes are influenced by water vapor and volcanic aerosols (Zhu et al. 2022; Solomon 1999; Zhu et al. 2018; de F. Forster and Shine 1999). In WACCM4, the temperature change due to volcanic aerosols is calculated in a similar way to Tilmes et al. (2009) following the Chemistry–Climate Model Validation 2 (CCMVal2) protocols. WACCM4 has been shown to accurately represent stratospheric dynamics, the mean meridional circulation of constituents, and dynamical variability (Eyring et al. 2010; Marsh et al. 2013; Hurrell et al. 2013). We follow the standard FW2000 model setup provided by NCAR, where aerosols are set to the climatological volcanic aerosol surface area density (SAD) based on observations for the year 2000 (Eyring et al. 2010), which is much lower than what would be ejected by any major volcanic eruption. Similarly, the concentration of greenhouse gases and halogens follow the seasonal cycle of year 2000. The setup used in this study does not include the 11-year solar cycle and the Quasi-Biennial Oscillation (QBO) package is not activated, however our free running simulations include an internally generated QBO. We repeat here that we do not include aerosol emissions related to the HTHH eruption.

The control experiment is forced with climatological sea surface temperatures averaged over 1982–2001 from the merged between Hadley-NOAA/Optimal Interpolation SST analyses (Hurrell et al. 2008). The control experiment is integrated for 43 years, and we use the results from last the 38 years to form a 29-member ensemble (i.e., each 1st January is treated as the start of an individual ensemble member). The ensemble members are integrated for 10 years. To examine the response to a sudden increase in

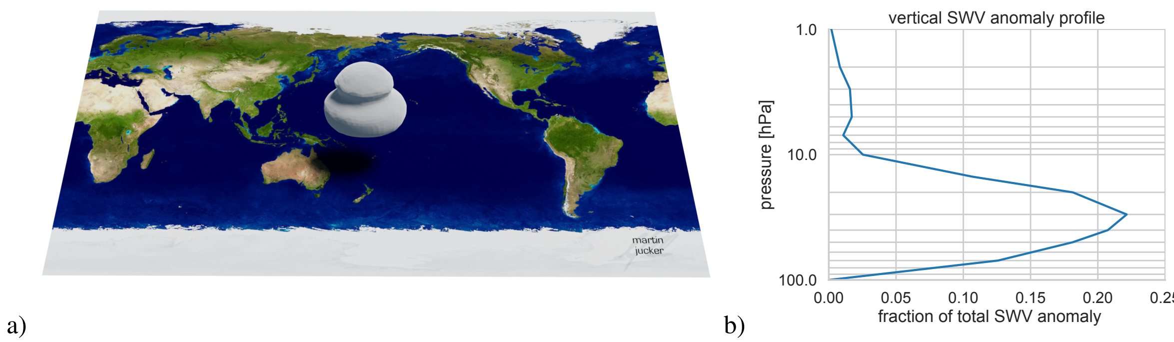

FIG. 1. a) Artist's view of the stratospheric water vapor cloud perturbation added at the start of each perturbation member simulation. b) Vertical profile of the initial cloud above the eruption as derived from MLS.

stratospheric water vapor, we restart each of the 29 ensemble members with a Gaussian water vapor anomaly centered at 20°S and 181°E (Fig. 1). Specifically, a majority of the SWV mass (94%) is placed between 22 and 27 km altitude, with a smaller concentration near 37 km. Horizontally, a Gaussian distribution is implemented with a latitudinal width of 5° and a longitudinal width of 10°.

We inject 125 Tg instead of the target 100 Tg of water vapor in the initial conditions, because about 20% are lost during the first few days due to the production of ice clouds, which we attribute to several factors connected to the idealized perturbation, such as the missing accompanying temperature perturbation, and the strong localization of the plume over only a few model grid points. The ice cloud disappears within a few days, after which the total stratospheric water anomaly approaches the targeted 100 Tg.

As the restarts are synchronized at the beginning of the year, the anomalies are also added on January 1st for each member. Branching a new perturbation member every year also allows us to sample the effect of the QBO, with 14 members in the easterly (QBOE) and 15 members in the westerly (QBOW) phase, as defined by the sign of the zonal mean zonal wind between 5S and 5N at 50hPa (Dunkerton 1990). We note here that during the HTHH eruption, the real stratosphere was in a QBOE phase.

Despite using a full chemistry-climate model, this is still an idealized experiment and there are significant limitations on the interpretation of the response predicted here, particularly around the use of a climatological SSTs. However, we focus on surface impact over land masses, and the anomalous atmospheric circulations which are responsible for those signals over land. We also chose to favor a large number of ensemble members and longer simulations over a fully coupled ocean, as that addition would severely limit our capacity in terms of ensemble size and simulation length. In addition, recent work has shown that the ocean-atmosphere coupled version of CESM1 struggles to reproduce the surface impacts of volcanic eruptions, and may therefore not lead to better predictions (Wu et al. 2023).

2) MiMA

To alleviate some of the restrictions on atmosphere-ocean interactions, we run additional ensemble simulations with the Model of an idealized Moist Atmosphere (MiMA, Jucker and Gerber 2017), an intermediate-complexity moist general circulation model. The advantage of this model is that it includes an interactive mixed layer ocean, allowing for an estimate of how SSTs might be influenced by the SWV and ozone perturbations produced in WACCM.

MiMA is based on GFDL AM2.1 atmospheric model with a spectral dynamical core, which we run at T42 resolution (2.8 degrees) and 40 vertical levels up to 0.07 hPa. MiMA includes interactive water vapor including evaporation and condensation, and a simplified convection scheme following Frierson et al. (2007), but it does not include any representation of cloud physics. Full radiative transfer is computed with the Rapid Radiative Transfer Model RRTMG (Mlawer et al. 1997), but here we fix ozone and water vapor to the monthly values from our WACCM simulations (monthly means linearly interpolated to each radiation time step). We include a homogeneous CO_2 concentration of 390 ppm, the solar constant is set to 1370 Wm^{-2}, and surface albedo follows Garfinkel et al. (2020b) with a value of 0.23 at low latitudes and 0.80 in polar regions.

We run MiMA in a configuration following the Southern Hemisphere benchmark case of Garfinkel et al. (2020a), which most notably includes a gravity wave scheme and surface ocean heat fluxes mimicking the major ocean currents plus a realistic Intertropical Convergence Zone (ITCZ) and South Pacific Convergence Zone (SPCZ)

(Fig. S4). Land surface includes realistic topography, increased surface roughness, restricted evaporation, higher albedo (0.43) for the major deserts, and lower heat capacity (10 million $Jm^{-2}K^{-1}$ vs. 100-300 million $Jm^{-2}K^{-1}$ for water).

c. Statistical significance

Throughout the analysis, we compute anomalies as the difference between control and perturbation for each ensemble member, and then use a two-tailed t-test on the 29-member ensemble against the null hypothesis that the ensemble mean anomalies are zero. We have also used Kolmogorov-Smirnov and agreement of sign tests, and checked the results by using only half of the ensemble members and applying an additional bootstrapping test. The results are very similar in all cases. Rather than hatching significant regions, we only plot anomalies which are significant at the 90% confidence level. For bar plots, we estimate the 90% confidence interval from a 1000-sample bootstrap method.

d. Labeling of time

We add SWV perturbations on 1 January, meaning that calendar years are also a measure of years since eruption. We follow the convention that the year of the eruption is year 0, and 1 January one year after eruption is the start of year 1. With this convention, the years corresponding to the HTHH eruption are simply 2022+n for year n. We will mostly discuss seasonal means, and attribute December-January-February (DJF) to the year corresponding to January-February. That is, DJF of year 1 is December of year 0 to February of year 1, e.g., one year after eruption. DJF of year 0 does not include December, and year 10 only includes December.

3. Stratospheric evolution

We first examine the evolution of the stratospheric perturbations induced by the SWV plume, and stratify the results by initial QBO phase (Fig. 2). The total SWV mass perturbation remains in the stratosphere for 7-8 years, and the initial evolution is different based on initial QBO phase. We note that during the eruption of HTHH in 2022, the stratosphere was in a QBOE phase. In WACCM, QBOE members retain more total water vapor mass than QBOW, and by November 2023, the observed SWV anomaly from MLS (Fig. 2, black) aligns closely with the QBOE ensemble mean from WACCM (purple dashed). As described in Supplementary SA, an exponential fit to the observed SWV anomaly leads to a similar estimate of the anomaly lifetime of 7-9 years. There are, however, stronger peaks in MLS during boreal winter of years 1 and 2 compared to our simulations; on further inspection, we attribute those seasonal peaks in MLS to enhanced tropical convection

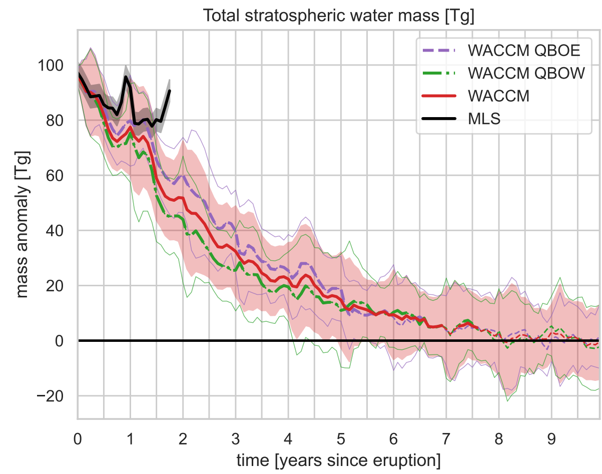

FIG. 2. Total stratospheric water vapor mass anomaly [Tg] for (red, solid) all WACCM members, (purple, dashed) QBOE members, (green, dash-dotted) QBOW members, and (black, solid) MLS (until 10 November 2023). Red shading and purple/green thin lines show the $\pm 1\sigma$ range across members. The ensemble mean is solid where statistically significant, and dashed otherwise.

which is independent of HTHH during this time in the observational dataset (see Fig. S5).

The differences in circulation between QBO phases result in distinct evolutions of the SWV anomaly during the first 2-3 years (Fig. 3). The members in the easterly phase (QBOE, those similar to HTHH) are subject to a weaker BDC and easterly tropical winds during the initial phase, and accumulate more SWV in the tropical stratosphere during the first year. They then also transport more SWV from the tropics into the NH during boreal winter one year after eruption (Schoeberl et al. 2023b, also see Fig. 5c). During the second year, when the members which were initially in the QBOE phase switch to QBOW and vice versa, the picture is inverted, and more SWV is transported towards Antarctica to influence the ozone hole, while more SWV accumulates in the tropical stratosphere for the (initially) QBOW members. Most of the SWV differences between the two QBO phases disappear by the end of year 3.

Besides differences in spatial distribution of SWV, the differences in total SWV mass between QBOE and QBOW members seen in Fig. 2 can be explained by the removal of SWV via development of polar stratospheric clouds (PSCs, Fig. 4). While QBOE members do not show any statistically significant increase in PSCs in either hemisphere (Fig. 4a), the QBOW members produce significantly more PSCs in the SH autumn of years 1 and 2 (Fig. 4b). As discussed above, QBOE members initially transport more SWV into the NH, leaving less SWV in the SH to produce PSCs. For QBOW members, the increased concentration of SWV remaining in the SH means that more PSCs form, and more SWV mass is lost to the formation of clouds. In

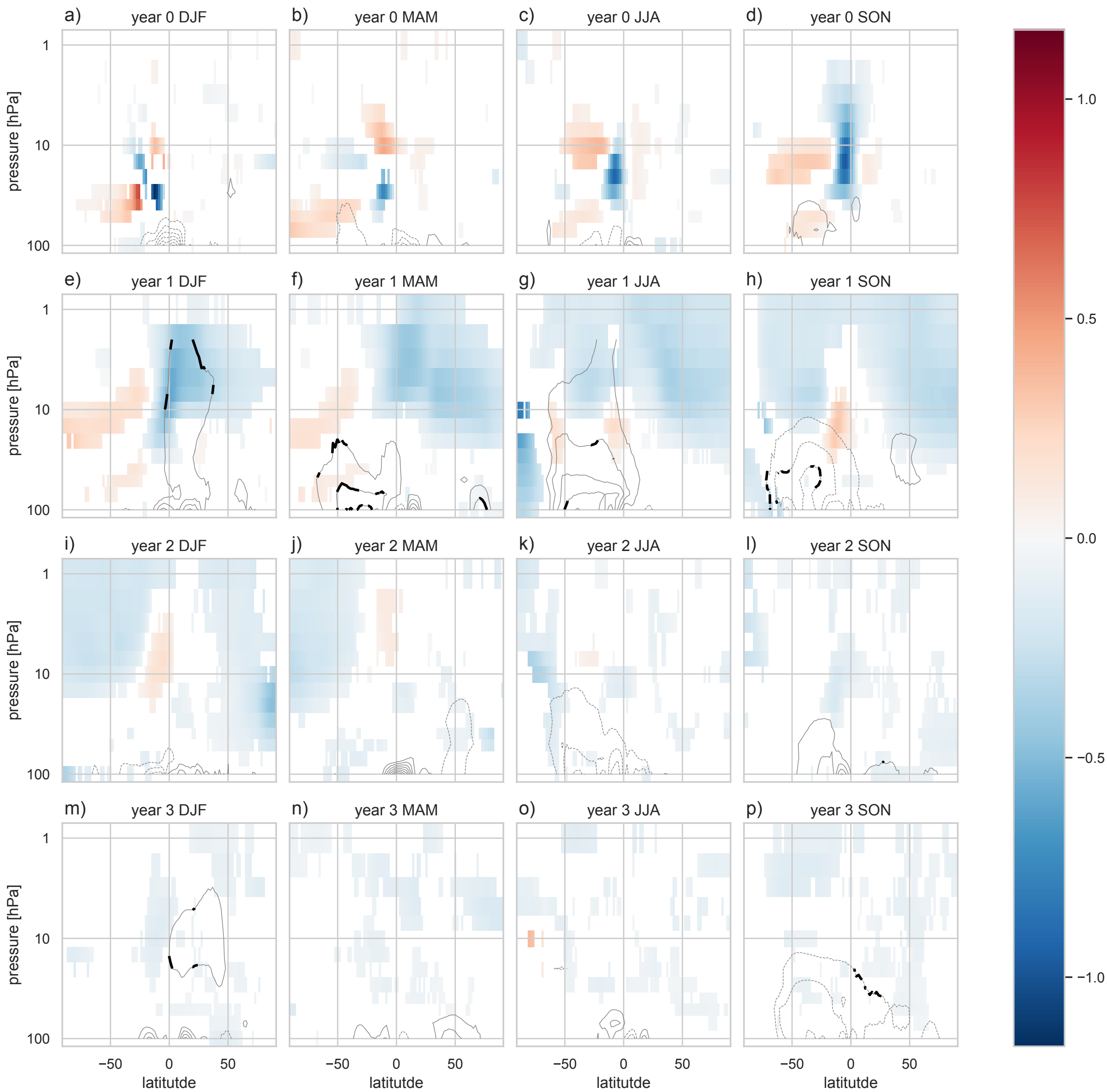

FIG. 3. Difference in (shading) water vapor and (contours) residual streamfunction between QBOW and QBOE ensemble members. Sign convention is such that blue shading means QBOE members (as in 2022) show more SWV, and dashed contours in the SH mean weaker BDC for QBOE members. Shading is only shown where statistically significant, contours are drawn in thick lines where significant. Contour interval is 10^8 kg/s, and SWV is in ppmv.

agreement with Fig. 3, the differences between QBOW and QBOE phases disappears during year 3.

Even though there are more PSCs in autumn for QBOW members, the ozone hole area is significantly larger during the second spring/summer after eruption for QBOE members (Fig. 5). This is because Antarctic total column ozone reduction happens over an extended period into early summer for QBOE members, while it is limited to mid-winter and midlatitudes for QBOW members (Fig. 5, bottom, black contours). We therefore expect a larger Antarctic ozone hole during the second spring/summer, which translates to 2023/24 if applied to the HTHH eruption, with a December mean increase of more than 2 million km^2 (Fig. 5a). The reason why the ozone hole is not significantly larger in year 1 already is that there is not enough time for the SWV to reach polar latitudes before the year 1 Antarctic polar vortex forms, and SWV can therefore not penetrate the polar vortex during the first year. How-

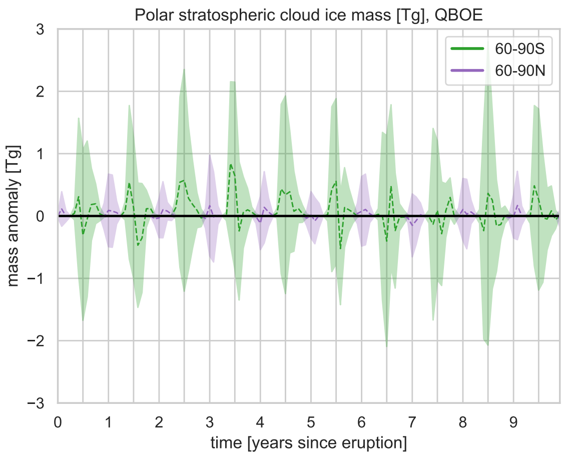

a)

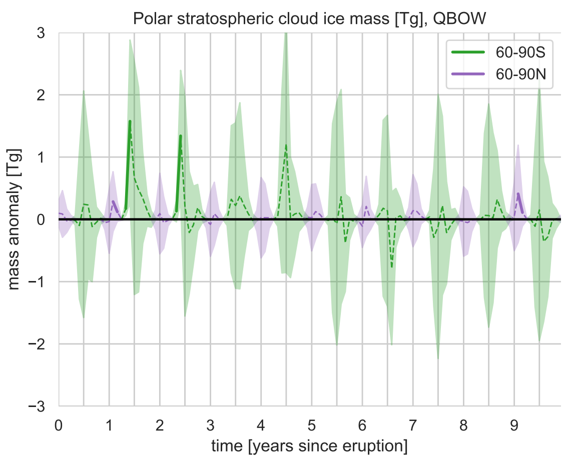

b)

FIG. 4. Total stratospheric polar ice cloud mass anomalies for (green) Antarctica and (purple) Arctic computed poleward of 60N/S for (a) QBOE and (b) QBOW ensemble members. Lines denote ensemble means, shading $\pm 1\sigma$, and lines are continuous if the ensemble mean is statistically significant.

ever, during the first DJF after eruption, SWV reaches high southern latitudes, and an increased ozone hole therefore forms during the following spring/summer (Fig. 5c). This is consistent with observations of both water vapor and ozone anomalies discussed by Manney et al. (2023), and with the large ozone hole observed in late spring of 2023 (above the 90$^{\text{th}}$ percentile at the time of writing[1]).

4. Tropospheric and surface impact

For the remainder of this article, we will focus on the seasonal impacts within the troposphere. The seasonal timescale is where anomalies start to become significant, while monthly data is too noisy for a meaningful analysis, and 6- and 12-month averages start washing over the seasonal signals (Fig. S6).

[1]`ozonewatch.gsfc.nasa.gov`; retrieved 30 November 2023

There is a well documented link between the strength of the Antarctic polar vortex, the size and duration of the ozone hole, and the phase of the Southern Annular Mode (SAM) during the following summer (Baldwin and Dunkerton 2001; Thompson et al. 2005; Lim et al. 2018); a strong polar vortex is more isolated and colder, creating favorable conditions for ozone depletion. A cold and more stable polar vortex also tends to break down later in the year, and is followed by a positive SAM during the following summer (Byrne and Shepherd 2018; Ceppi and Shepherd 2019). From this prior knowledge and the impact of the SWV perturbation on the Antarctic ozone hole discussed above (Fig. 5), we expect a positive SAM to develop two years after eruption for QBOE members.

This is indeed the case, as seen two years after eruption (2023/24 for HTHH) for QBOE members in the anomalous geopotential height field at 300 hPa (Fig. 6QBOE-a); although not statistically significant throughout all longitudes, there is a clear positive SAM signature with the characteristic dipole structure between middle and high southern latitudes during that year, and only for QBOE members.

As seen in Fig. 6, areas of statistically significant yearly anomalies are quite small for most years, and we will now focus on multi-year (years 3-7) mean anomalies, and justify that choice after the fact. For now, suffice to say that years 3-7 are the years with the most statistically significant anomalies.

Earlier studies have estimated the surface temperature impact of SWV anomalies using various scenarios (Solomon et al. 2010; Maycock et al. 2013; Huang et al. 2016, 2020; Li and Newman 2020). Most studies have found only small effects on global temperatures, including Jenkins et al. (2023) who estimated the global mean surface temperature effect of the HTHH SWV anomaly to be 0.035°C. Our results align closely with those estimates with a global mean averaged near-surface temperature anomaly (2-meter temperature) of 0.015±0.031°C averaged over years 3-7. However, we have fully consistent WACCM simulations which include radiation, dynamics, and chemistry, and we can therefore perform a detailed analysis of regional surface impacts.

Averaged over those five years, there are substantial surface temperature anomalies over the Northern Hemisphere during winter and spring, reaching above 1.5°C over large areas of North America in DJF and close to 1.5°C over central Eurasia in MAM (Fig. 7a,b). There is also a cold anomaly over Scandinavia in DJF, and the Arctic is anomalously warm over most of the year, but most importantly during SON (Fig. 7a-d). Note that our simulations do not include interactive sea-ice, but these long-term Arctic temperature anomalies should be expected to impact sea-ice extent and concentrations, which would then also positively feedback onto Arctic temperatures via albedo feedback. In the Southern Hemisphere, the main surface

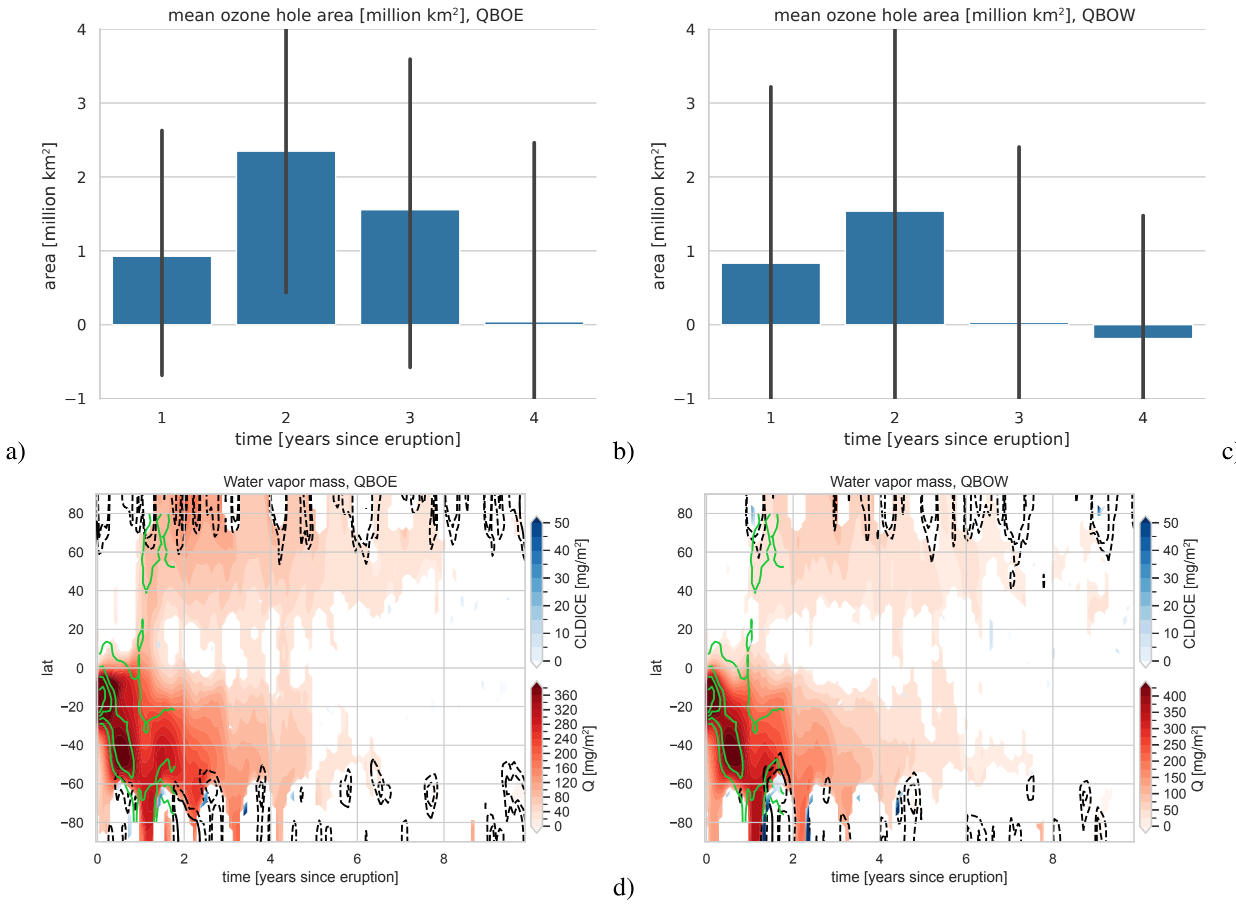

FIG. 5. (top) December anomalous Antarctic ozone hole area, as defined by the area where total column ozone is below 220 DU for a) QBOE and b) QBOW members. Error bars denote the 90% confidence interval. (bottom) Total anomalous stratospheric water vapor (red shading) and cloud ice (blue shading) mass [mg/m^2] above 100 hPa, and total column ozone anomalies (black contours, -10 and -5 DU, solid where significant). Shading is only shown where significant. MLS data until 10 November 2023 in green and a contour interval of 250 mg/m^2. c) for QBOE members, d) for QBOW members.

temperature anomalies are found over Australia, where the local winters are almost 1°C cooler, and in the Amundsen Sea, which is about 0.5°C warmer (Fig. 7c). In addition, Western Australia also has slightly lower temperatures in summer and autumn(Fig. 7a,b).

The main regions of significant rainfall anomalies are located in the Pacific (most prominent in DJF) and in the Indian Ocean in JJA (Fig. 7e-h). There is an indication of a wave train emanating from the tropical Pacific north and east towards North America in DJF (Fig. 7e), and a similar wave train starting in the northern Indian Ocean going south and east in JJA (Fig. 7g). In DJF and over land, Europe and Western Australia receive slightly more precipitation than usual, while the West Coast US is drier than usual (Fig. 7e). In JJA, land anomalies include drier summers over northern Eurasia, and wet anomalies along China's east coast and over northern Australia (Fig. 7g).

We now consider the year-by-year evolution of surface anomalies within selected regions (rectangular boxes in Fig. 7). Besides showing more temporal detail, this also allows to justify our choice of year 3-7 averaging.

Fig. 8 confirms that the regional anomalies have a general tendency to be largest during years 3-7. We also note that by year 3, the differences between QBOE and QBOW members are not significant (Fig. 3), and we use all members from here on.

The North American surface temperature anomalies are the highest, and gradually increase until they peak at around 1.8°C (area average) during year 4 (Dec 2025 - Feb 2026 for HTHH) (Fig. 8a, green). The largest negative anomalies are over Scandinavia and Australia, and they peak around the same period (Fig. 8a, blue for Scandinavia, Fig. 8c, blue for Australia). The Australian anomalies are also the most persistent, with significant cooling from year 1 (JJA 2023) to 8 (JJA 2030).

For precipitation, there is a clear dipole developing between a drier northern tropical Central Pacific (Fig. 8e, blue) and a wetter northern tropical Western Pacific

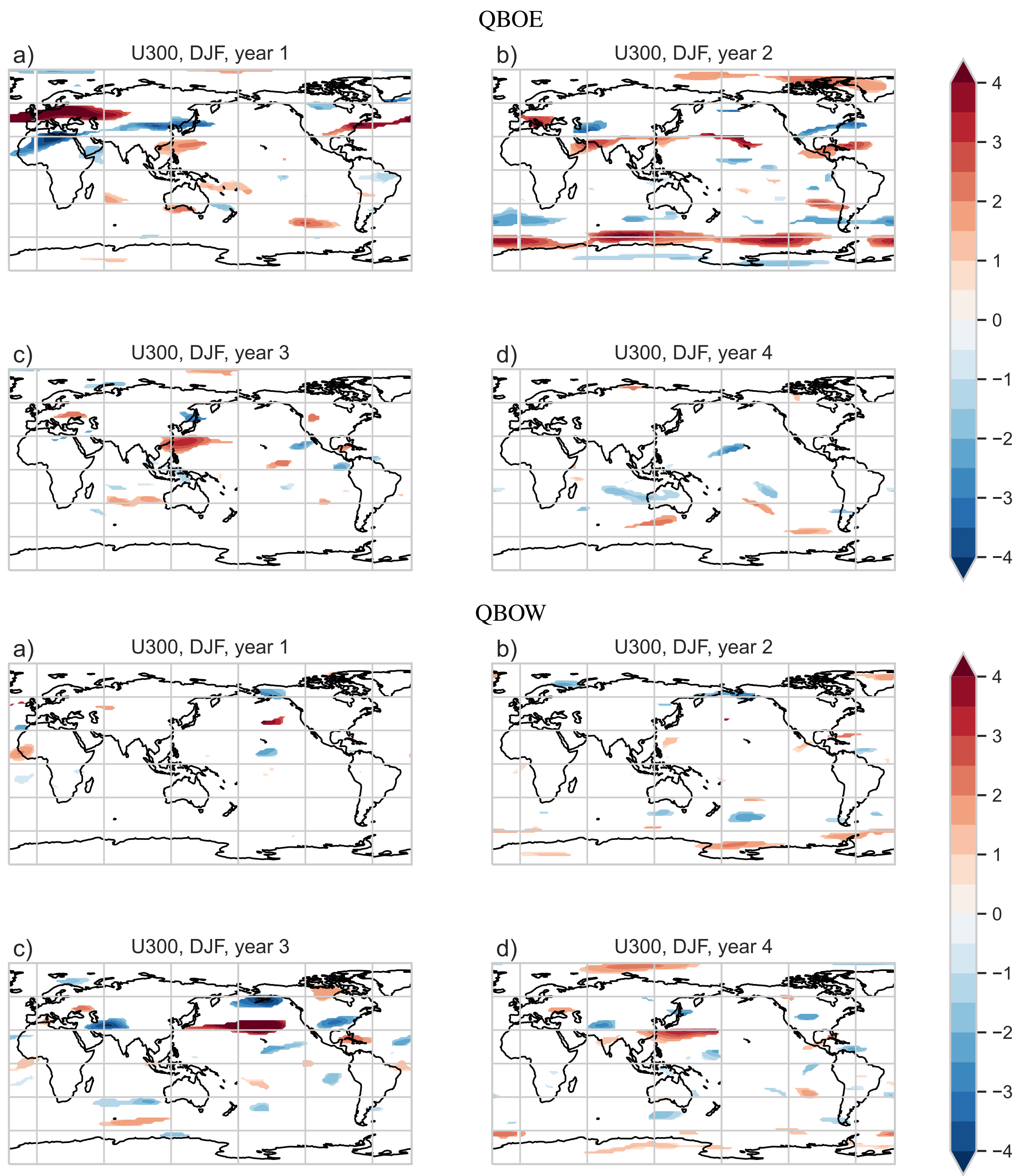

FIG. 6. 300 hPa zonal wind anomalies for (top) QBOE and (bottom) QBOW members [m/s].

(Fig. 8e, orange) in DJF. In JJA, the Indian Ocean shows a dipole between the northern and southern tropical regions (Fig. 8f), with the northern edge around the Indian subcontinent wetter and the tropical Indian Ocean just south of the equator anomalously dry. These dipoles are similar to the typical anomalies related to El Niño and the Indian Ocean Dipole, even though our simulations do not include interactive SSTs. Nevertheless, we will come back to the global importance of these oceanic anomalies below.

5. Analysis

We now want to understand how those surface anomalies develop, and focus on the two respective winter seasons DJF and JJA, as those are the two seasons with the strongest surface temperature and precipitation anomalies in the two hemispheres. The simplest explanation for changes in surface temperature forced by the SWV anomalies is a stronger greenhouse effect causing surface heating. There is a clear match between the regions of anomalous heat in the NH

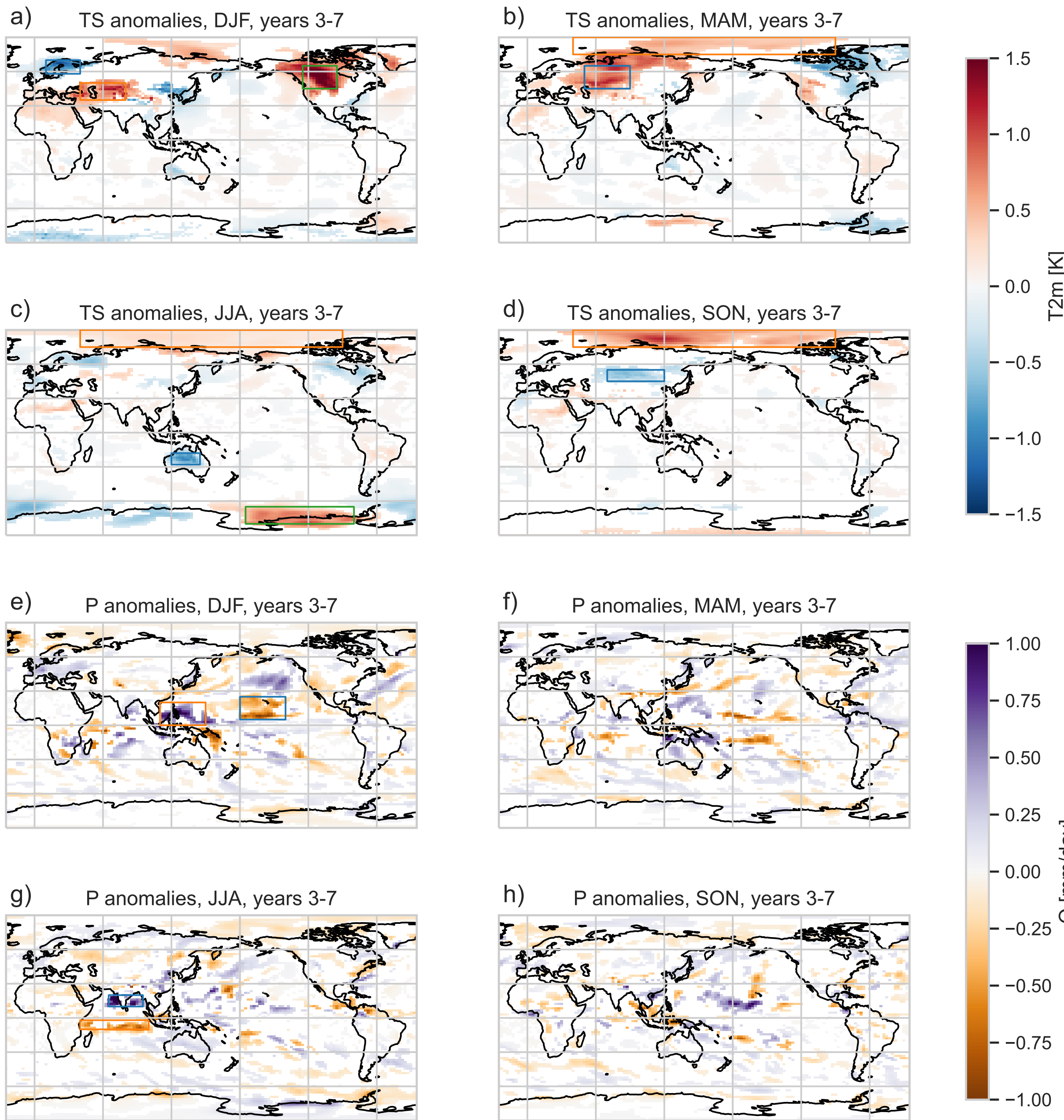

Fig. 7. Year 3-7 seasonal mean anomalies for (top) 2m temperature and (bottom) precipitation, during (a,e) DJF, (b,f) MAM, (c,g) JJA, and (d,h) SON. Only statistically significant anomalies are shown.

during DJF as shown in Fig. 7, and longwave forcing, as those regions receive anomalous downwelling longwave radiation at the surface during that season (Fig. 9a; note this includes tropospheric water vapor but not cloud forcing). A similar conclusion can be drawn regarding Arctic warming in JJA (Fig. 9b).

The strong regional character of the heating and cooling patterns suggest that cloud and dynamical effects are important in setting up the surface response to the SWV perturbations. Cloud feedbacks play a dominant role in setting up the cooling over Australia and warming over the Amundsen Sea during years 3-7, as there are increases in cloud fraction in these regions (Fig. 9d). The cooling over Australia can therefore be linked to shortwave cloud forcing (Fig. 9h) which matches the patterns of surface cooling (Fig. 7), while the warming in the Amundsen Sea

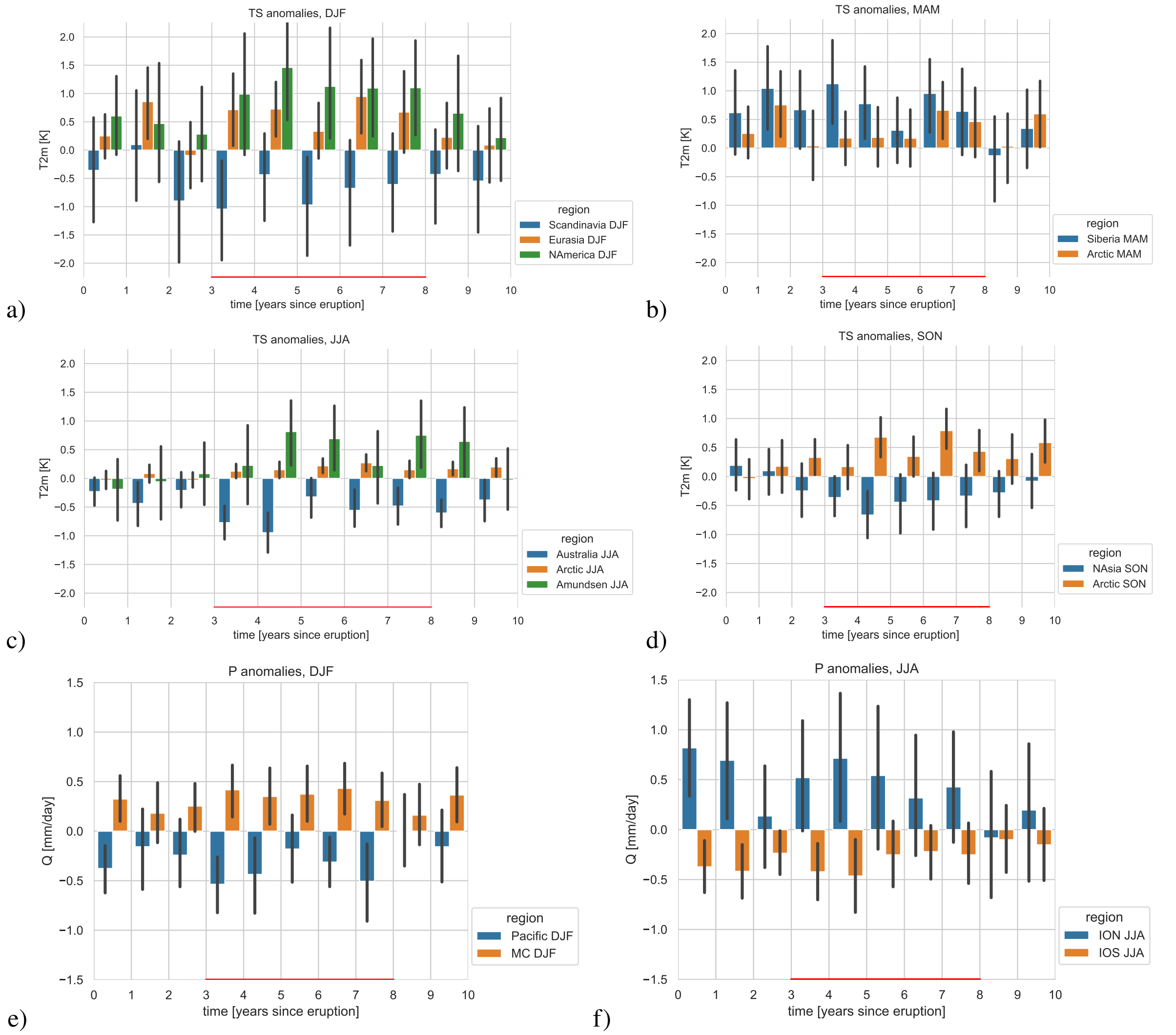

FIG. 8. Year-by-year seasonal anomalies for the regions indicated by boxes in Fig. 7 for (a-d) surface temperature and (e,f) precipitation, and (a,e) DJF, (b) MAM, (c,f) JJA, (d) SON. The red horizontal lines denote the averaging period for years 3-7. All members are used, and error bars denote the 90% confidence intervals. Refer to legend for region and season. Colors are the same as the corresponding boxes in Fig. 7. See Fig. S6 for timeseries for each region.

is at least partially due to increased longwave cloud forcing (Fig. 9f). Cloud forcing also matches the precipitation response in the extratropical Pacific, where decreases in precipitation are accompanied by fewer clouds, resulting in positive cloud shortwave (more sunlight reaches the surface) and negative cloud longwave forcing (less surface longwave emission is being blocked; Fig. 9ceg). Cloud anomalies are also consistent with the increase in precipitation over Europe in DJF (Fig. 7b), as the same region shows increased cloud cover and cloud forcing (Fig. 9ceg).

Interestingly, there are only minor cloud effects in the regions of land surface warming in the NH. Furthermore, cloud forcing even counteracts the greenhouse heating of SWV over the arctic (Fig. 9h, green area in the Arctic), and there is less cloud cover accompanied by net positive cloud forcing anomalies over the east coast of China and southern parts of North America ([Fig. 9ceg), where the surface cools rather than warms. These observations suggest that dynamical effects are also important.

To assess the dynamical feedbacks to the imposed SWV forcing, recall that there are strong precipitation anomalies in the Pacific in DJF and the Indian Ocean in JJA (Fig. 7). The northern Pacific DJF anomalies suggest a wave train originating in the tropical Central Pacific heading north east towards North America (Fig. 7e). A clear wave pattern originating over the Pacific can be seen in 350 K potential vorticity anomalies and wave activity flux (Fig. 10). A similar pattern is also seen in other dynamical

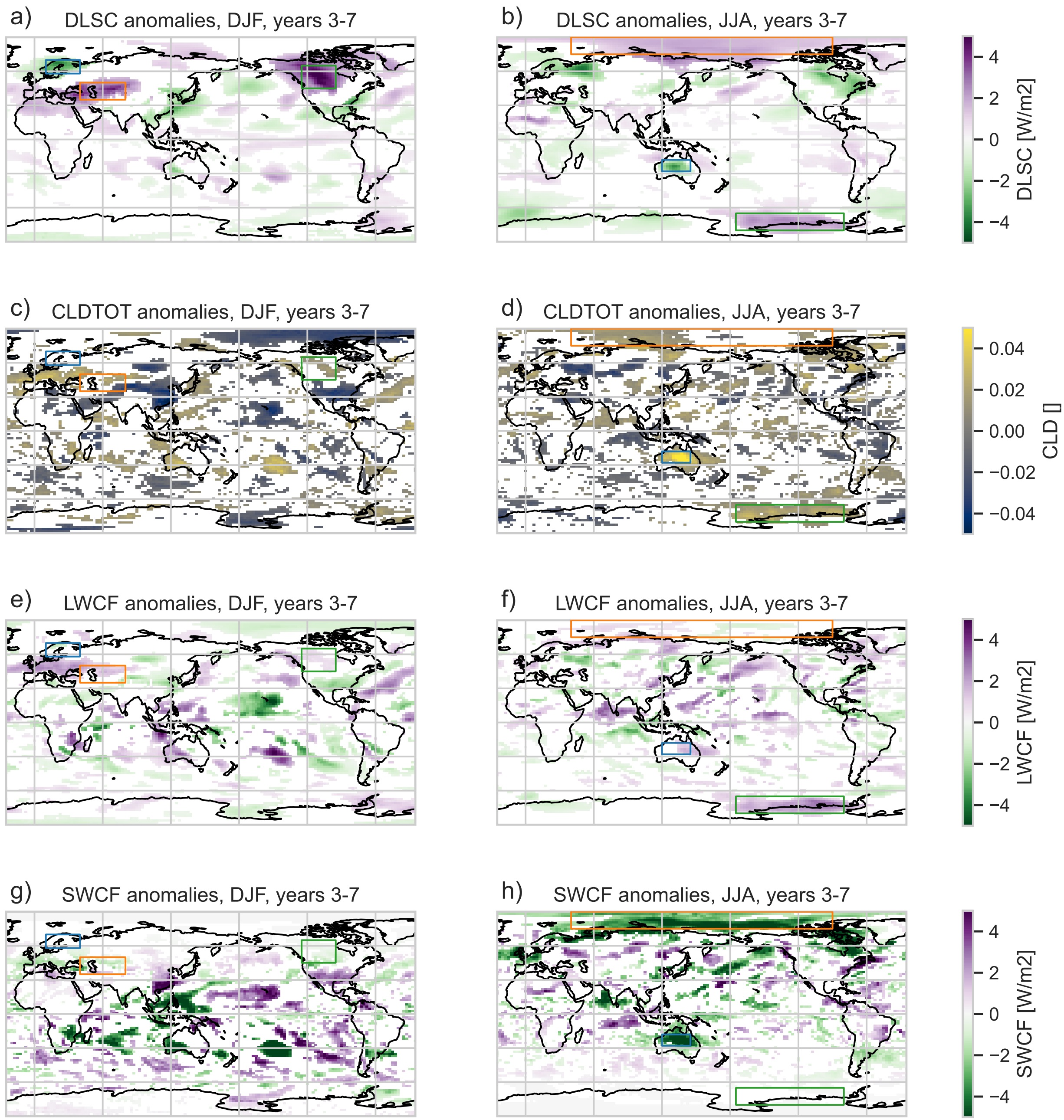

FIG. 9. Same as Fig. 7, but for DJF (left) and JJA (right) only, and for (a,b) clear-sky downwelling longwave radiation at the surface (DLSC), (c,d) total cloud fraction, (e,f) longwave cloud forcing (LWCF), and (g,h) shortwave cloud forcing (SWCF). The same boxes as in Fig. 7a,d are overlaid for easier comparison.

variables, such as 300 hPa meridional and zonal wind or geopotential height (Fig. S7). Thus, in DJF a stationary wave pattern is established over the NH extratropics, with anticyclonic PV anomalies over regions showing warming, and cyclonic anomalies where the surface cools. Another consequence of this global wave train is a strengthening of the zonal jet over Europe, which accompanies the increased cloud cover and rainfall described earlier (Fig. S7, bottom). In contrast, there is no clear circumglobal wave pattern in the SH, nor in JJA. However, there is an increase in wave activity flux towards the Amundsen Sea in JJA (Fig. 10b) which coincides with meridional wind anomalies (Fig. S7, middle), increased cloud cover (Fig. 9d) and surface warming (Fig. 7c), confirming the importance of

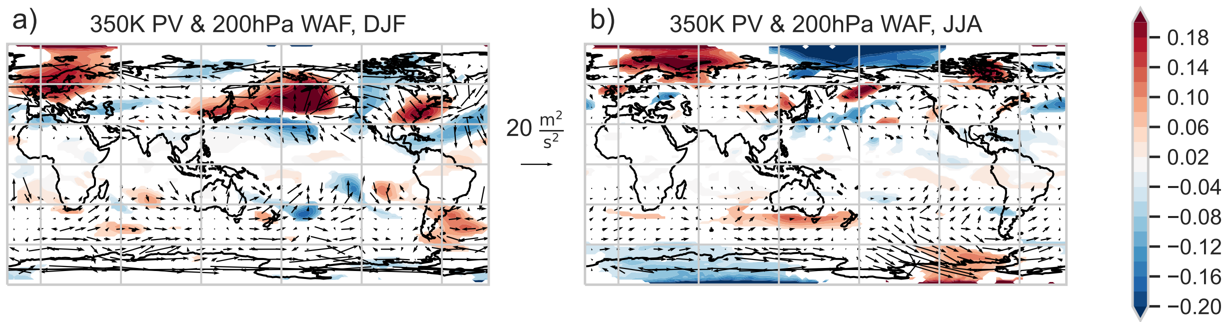

FIG. 10. Potential vorticity at the 350K isentrope (shading, in PVU) and horizontal wave activity flux (arrows) for (a) DJF and (b) JJA. Only statistically significant values are shown, and arrows within 15S-15N and outside 80S/N are masked for clarity. Both quantities are averaged from year 3 to 7 as before.

dynamical tropospheric feedbacks in setting up surface anomalies globally.

Idealised simulations

In order to assess possible impacts of the SWV anomalies on SSTs, we ran additional simulations with the Model of an idealized Moist Atmosphere (MiMA, Jucker and Gerber 2017), as described in Section 2b. As a reminder, these simulations are forced by WACCM SWV and ozone in the radiative transfer calculations, and include an interactive mixed layer ocean. Thus, we can estimate the radiative impact of the SWV anomaly on surface temperatures around the globe (excluding cloud feedbacks). We note that as described by Jucker (2019) and Garfinkel et al. (2020b), due to various simplifications in the model the seasonal cycle at the surface is somewhat lagging compared to comprehensive models, and therefore some features appearing in DJF in WACCM may leak into MAM in MiMA, and similarly for JJA and SON.

Global mean surface temperature anomalies (including SSTs) are 0.032±0.022°C with this model, which is again very close to the 0.035°C estimated by Jenkins et al. (2023). Regional surface temperature anomalies from these simulations show a clear picture of warming winter hemisphere landmasses, and cooling summer hemisphere landmasses (Fig. 11). We note that additional simulations where only ozone or only SWV anomalies where added suggest that the surface temperature signal is dominated by SWV, and ozone has only minor impact in these simulations (Figs. S9 and S10). The MiMA simulations confirm the robustness of the SWV-induced wave structure in the Pacific (Fig. 11ef), and they produce tropical surface temperature anomalies consistent with an El Niño-like pattern (Fig. 11a-d). This heating is produced by the zonally asymmetric distribution of SWV in the tropics, and consistent with the increased surface downward longwave flux over the tropical Pacific in WACCM (Fig. 9a). Thus, it is possible that the SWV forcing from the eruption would favor a positive phase of ENSO on a multi-year timescale, potentially by influencing tropical convection via changes in static stability in the tropics (e.g., Rao et al. 2023). Further work is required to confirm this, which we leave for a follow-up study.

On the other hand, these simulations confirm the importance of cloud feedbacks, as the regions observed to suffer cooling in winter in the WACCM simulations (Scandinavia, Australia) consistently warm together with the rest of the winter hemisphere in the cloud-less MiMA simulations (Fig. 11a-d). The cooling of the summer hemisphere land masses in MiMA is consistent with the widely absent warming in WACCM in that season, and we attribute it to increased shortwave absorption in the stratosphere due to enhanced SWV levels (see Fig. S11).

The MiMA simulations also show circumglobal wave trains, although their structure is qualitatively different to the wave trains discussed for the WACCM simulations (Fig. S8). This is to be expected, as the warming and cooling in each hemisphere is more zonally symmetric in MiMA, and missing cloud feedbacks and simplified convection can be expected to have an influence on storm track behavior (Ceppi and Hartmann 2016; Fuchs et al. 2022). Even so, the MiMA simulations provide evidence of the robustness of the surface impacts from our SWV perturbation simulations with WACCM discussed above.

6. Summary and Conclusions

Our analysis uses the eruption of Hunga-Tonga Hunga Ha'apai (HTHH) as a base case to show that anomalies in stratospheric water vapor (SWV) concentrations can have significant impacts on the climate system. Neglecting the relatively small aerosol forcing from HTHH, we find that such large SWV anomalies can increase the ozone hole area during the second spring/summer after eruption, and force a positive Southern Annular Mode over the following austral summer. However, the impact on the Antarctic ozone hole depends on the phase of the Quasi-Biennial

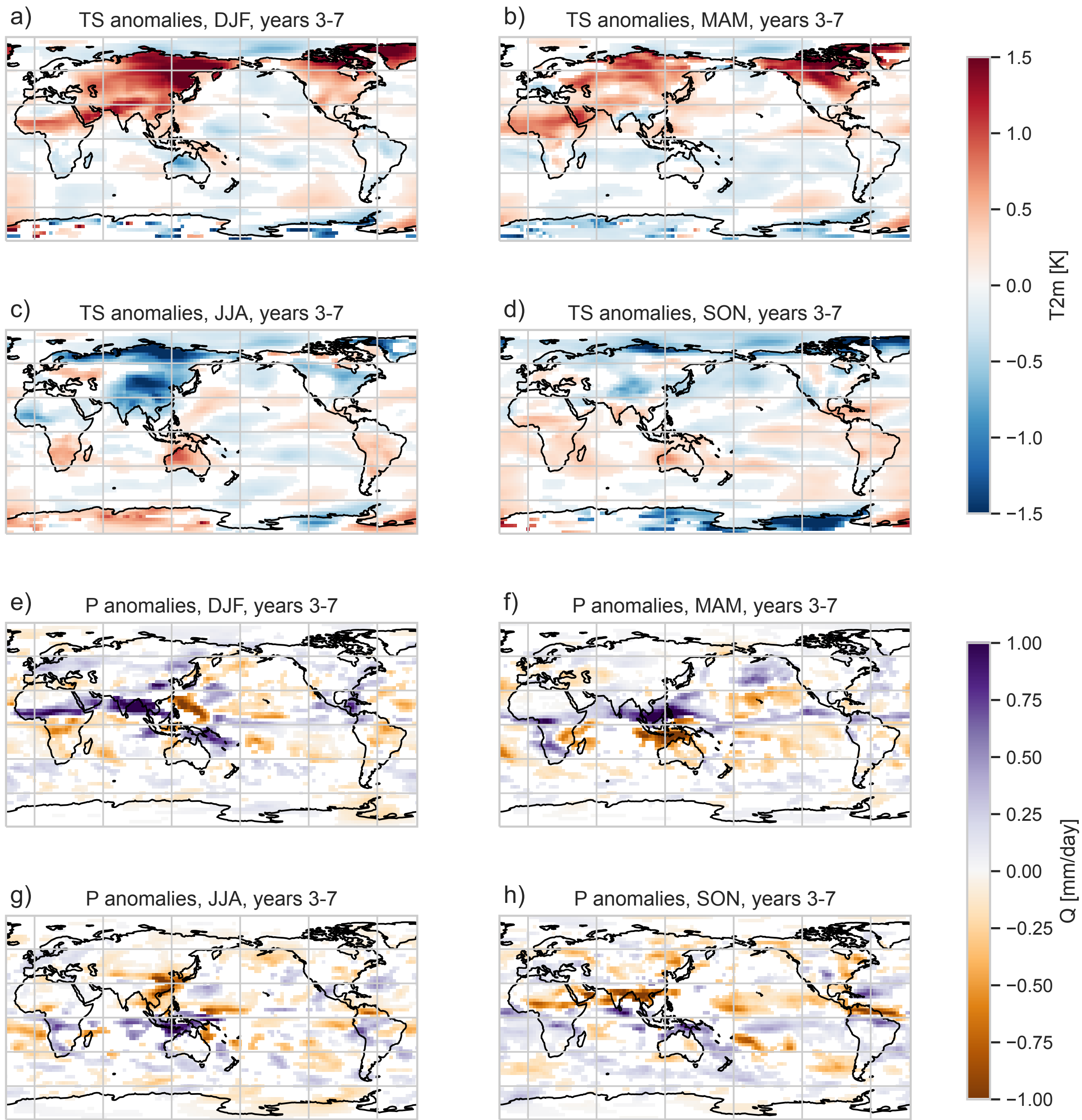

FIG. 11. As Fig. 7, but for MiMA simulations: (a-d) Surface temperature and (e-h) precipitation anomalies.

Oscillation (QBO) around the time of the eruption, with the easterly phase (QBOE) showing more impact than the westerly phase (QBOW). For QBOE (as was the case during the HTHH eruption), we obtain an ensemble mean, December mean ozone hole area increase of more than 2 million km^2. The effect of the initial QBO phase vanishes by year 3.

Our WACCM simulations reveal significant surface temperature and precipitation anomalies globally which peak around years 3-7 after the initial water vapor plume was injected into the stratosphere, e.g., years 2025-2029 for HTHH, but can already appear earlier. The Northern Hemisphere experiences substantial surface temperature anomalies during winter and spring, with strong warming over North America and central Eurasia, and cooling over Scandinavia. The Arctic also exhibits anomalous warmth throughout the year, particularly during the September-November period. In the Southern Hemisphere, cool anomalies are observed over Australia, while the Amundsen Sea is warmer than usual.

Precipitation anomalies are found in the Pacific and Indian Oceans, with indications of wave trains originating from the tropical Pacific and Indian Ocean. Europe and Australia receive increased precipitation in winter, while the West Coast US is drier than usual. In summer, northern Eurasia experiences drier conditions, while China's east coast and western Australia see wet anomalies.

Through further analysis, we determine that cloud and dynamical effects play important roles in setting up the surface response to the SWV perturbations. Cloud feedbacks contribute to the cooling over Australia and the warming in the Amundsen Sea, while a circumglobal wave train in northern winter midlatitudes contributes to temperature anomalies of both signs across all longitudes, and the increased rainfall over Europe.

Additional simulations with an idealized model with interactive mixed layer ocean indicate that the Pacific anomalies seen in WACCM might be accompanied by a positive tendency of the El Niño Southern Oscillation, but further work needs to be done to confirm this link.

Acknowledgments. MJ was supported by the ARC Centre of Excellence for Climate Extremes which is supported by the Australian Research Council via grant CE170100023. This research was undertaken with the assistance of resources from the National Computational Infrastructure (NCI Australia), an NCRIS enabled capability supported by the Australian Government. Additional computing resources were provided through the ARC LIEF grant LE200100040.

Data availability statement. All analysis scripts will be made on github.com upon acceptance. Similarly, we will make the post-processed simulation data as well any configuration files for the models to duplicate our simulations openly available via zenodo.com. Any direct access to full simulation data can be arranged by contacting the authors.

References

Baldwin, M. P., and T. J. Dunkerton, 2001: Stratospheric harbingers of anomalous weather regimes. *Science (New York, N.Y.)*, **294 (5542)**, 581–4, https://doi.org/10.1126/science.1063315, URL http://www.ncbi.nlm.nih.gov/pubmed/11641495.

Baldwin, M. P., and Coauthors, 2001: The quasi-biennial oscillation. *Reviews of Geophysics*, **39 (2)**, 179, https://doi.org/10.1029/1999RG000073, URL http://doi.wiley.com/10.1029/1999RG000073http://www.agu.org/pubs/crossref/2001/1999RG000073.shtml.

Brewer, A., 1949: Evidence for a world circulation provided by the measurements of helium and water vapour distribution in the stratosphere. *Quarterly Journal of the Royal Meteorological Society*, **75 (326)**, 351–363, https://doi.org/10.1002/qj.49707532601, URL http://onlinelibrary.wiley.com/doi/10.1002/qj.49707532603/abstracthttp://doi.wiley.com/10.1002/qj.49707532601.

Byrne, N. J., and T. G. Shepherd, 2018: Seasonal Persistence of Circulation Anomalies in the Southern Hemisphere Stratosphere and Its Implications for the Troposphere. *Journal of Climate*, **31 (9)**, 3467–3483, https://doi.org/10.1175/JCLI-D-17-0557.1, URL http://journals.ametsoc.org/doi/10.1175/JCLI-D-17-0557.1.

Carn, S. A., N. A. Krotkov, B. L. Fisher, and C. Li, 2022: Out of the blue: Volcanic SO2 emissions during the 2021–2022 eruptions of Hunga Tonga—Hunga Ha'apai (Tonga). *Frontiers in Earth Science*, **10**, https://doi.org/10.3389/feart.2022.976962, URL https://www.frontiersin.org/articles/10.3389/feart.2022.976962/full.

Carr, J. L., A. Horváth, D. L. Wu, and M. D. Friberg, 2022: Stereo Plume Height and Motion Retrievals for the Record-Setting Hunga Tonga-Hunga Ha'apai Eruption of 15 January 2022. *Geophysical Research Letters*, **49 (9)**, https://doi.org/10.1029/2022GL098131, URL https://onlinelibrary.wiley.com/doi/10.1029/2022GL098131.

Ceppi, P., and D. L. Hartmann, 2016: Clouds and the Atmospheric Circulation Response to Warming. *Journal of Climate*, **29 (2)**, 783–799, https://doi.org/10.1175/JCLI-D-15-0394.1, URL http://journals.ametsoc.org/doi/abs/10.1175/JCLI-D-15-0394.1http://journals.ametsoc.org/doi/10.1175/JCLI-D-15-0394.1.

Ceppi, P., and T. G. Shepherd, 2019: The Role of the Stratospheric Polar Vortex for the Austral Jet Response to Greenhouse Gas Forcing. *Geophysical Research Letters*, **46 (12)**, 6972–6979, https://doi.org/10.1029/2019GL082883, URL https://onlinelibrary.wiley.com/doi/abs/10.1029/2019GL082883.

de F. Forster, P. M., and K. P. Shine, 1999: Stratospheric water vapour changes as a possible contributor to observed stratospheric cooling. *Geophysical Research Letters*, **26 (21)**, 3309–3312, https://doi.org/10.1029/1999GL010487, URL http://doi.wiley.com/10.1029/1999GL010487.

Dessler, A. E., M. R. Schoeberl, T. Wang, S. M. Davis, and K. H. Rosenlof, 2013: Stratospheric water vapor feedback. *Proceedings of the National Academy of Sciences*, **110 (45)**, 18 087–18 091, https://doi.org/10.1073/pnas.1310344110, URL http://www.pnas.org/content/110/45/18087.abstract?sid=acfc4b60-a536-41dd-8504-290f25d16fe6http://www.pnas.org/cgi/doi/10.1073/pnas.1310344110https://pnas.org/doi/full/10.1073/pnas.1310344110.

Dobson, G. M. B., 1956: Origin and Distribution of the Polyatomic Molecules in the Atmosphere. *Proceedings of the Royal Society A: Mathematical, Physical and Engineering Sciences*, **236 (1205)**, 187–193, https://doi.org/10.1098/rspa.1956.0127, URL http://rspa.royalsocietypublishing.org/cgi/doi/10.1098/rspa.1956.0127.

Dunkerton, T. J., 1990: Annual Variation of Deseasonalized Mean Flow Acceleration in the Equatorial Lower Stratosphere. *Journal of the Meteorological Society of Japan. Ser. II*, **68 (4)**, 499–508, https://doi.org/10.2151/jmsj1965.68.4{_}499, URL https://www.jstage.jst.go.jp/article/jmsj1965/68/4/68_4_499/_article.

Eyring, V., T. G. Shepherd, and D. W. Waugh, 2010: SPARC CCMVal Report on the Evaluation of Chemistry-Climate Models. Tech. rep., SPARC, 426 pp. pp. URL http://www.sparc-climate.org/publications/sparc-reports/.

Frierson, D. M. W., I. M. Held, and P. Zurita-Gotor, 2007: A Gray-Radiation Aquaplanet Moist GCM. Part II: Energy Transports in Altered Climates. *Journal of the Atmospheric Sciences*, **64 (5)**, 1680–1693, https://doi.org/10.1175/JAS3913.1, URL http://journals.ametsoc.org/doi/abs/10.1175/JAS3913.1.

Fuchs, D., S. C. Sherwood, D. Waugh, V. Dixit, M. H. England, Y.-L. Hwong, and O. Geoffroy, 2022: Midlatitude jet position spread linked to atmospheric convective types. *Journal of Climate*, 1–44, https://doi.org/10.1175/jcli-d-21-0992.1.

Garfinkel, C. I., I. White, E. P. Gerber, and M. Jucker, 2020a: The Impact of SST Biases in the Tropical East Pacific and Agulhas Current Region on Atmospheric Stationary Waves in the Southern Hemisphere. *Journal of Climate*, **33 (21)**, 9351–9374, https://doi.org/10.1175/JCLI-D-20-0195.1, URL https://journals.ametsoc.org/doi/10.1175/JCLI-D-20-0195.1.

Garfinkel, C. I., I. White, E. P. Gerber, M. Jucker, and M. Erez, 2020b: The building blocks of Northern Hemisphere wintertime stationary waves. *Journal of Climate*, **33 (13)**, 5611–5633, https://doi.org/10.1175/JCLI-D-19-0181.1, URL http://journals.ametsoc.org/doi/10.1175/JCLI-D-19-0181.1.

Gupta, A. K., R. Bennartz, K. E. Fauria, and T. Mittal, 2022: Eruption chronology of the December 2021 to January 2022 Hunga Tonga-Hunga Ha'apai eruption sequence. *Communications Earth & Environment*, **3 (1)**, 314, https://doi.org/10.1038/s43247-022-00606-3, URL https://www.nature.com/articles/s43247-022-00606-3.

Guzewich, S. D., and Coauthors, 2022: Volcanic Climate Warming Through Radiative and Dynamical Feedbacks of SO 2 Emissions. *Geophysical Research Letters*, **49 (4)**, https://doi.org/10.1029/2021GL096612, URL https://agupubs.onlinelibrary.wiley.com/doi/10.1029/2021GL096612.

Holton, J. R., and H.-C. Tan, 1980: The Influence of the Equatorial Quasi-Biennial Oscillation on the Global Circulation at 50 mb. *Journal of the Atmospheric Sciences*, **37 (10)**, 2200–2208, https://doi.org/10.1175/1520-0469(1980)037⟨2200:TIOTEQ⟩2.0.CO;2, URL http://journals.ametsoc.org/doi/abs/10.1175/1520-0469%281980%29037%3C2200%3ATIOTEQ%3E2.0.CO%3B2.

Huang, Y., Y. Wang, and H. Huang, 2020: Stratospheric Water Vapor Feedback Disclosed by a Locking Experiment. *Geophysical Research Letters*, **47 (12)**, 1–8, https://doi.org/10.1029/2020GL087987.

Huang, Y., M. Zhang, Y. Xia, Y. Hu, and S. W. Son, 2016: Is there a stratospheric radiative feedback in global warming simulations? *Climate Dynamics*, **46 (1-2)**, 177–186, https://doi.org/10.1007/s00382-015-2577-2, URL http://dx.doi.org/10.1007/s00382-015-2577-2.

Hurrell, J. W., J. J. Hack, D. Shea, J. M. Caron, and J. Rosinski, 2008: A New Sea Surface Temperature and Sea Ice Boundary Dataset for the

Community Atmosphere Model. *Journal of Climate*, **21 (19)**, 5145–5153, https://doi.org/10.1175/2008JCLI2292.1, URL http://journals.ametsoc.org/doi/10.1175/2008JCLI2292.1.

Hurrell, J. W., and Coauthors, 2013: The Community Earth System Model: A Framework for Collaborative Research. *Bulletin of the American Meteorological Society*, **94 (9)**, 1339–1360, https://doi.org/10.1175/BAMS-D-12-00121.1, URL http://journals.ametsoc.org/doi/10.1175/BAMS-D-12-00121.1.

Jenkins, S., C. Smith, M. Allen, and R. Grainger, 2023: Tonga eruption increases chance of temporary surface temperature anomaly above 1.5 °C. *Nature Climate Change*, **13 (2)**, 127–129, https://doi.org/10.1038/s41558-022-01568-2.

Jucker, M., 2019: The Surface of an Aquaplanet GCM. URL https://research-iceberg.github.io/papers/M_Jucker_201907/, https://doi.org/10.5281/zenodo.3358284.

Jucker, M., and E. P. Gerber, 2017: Untangling the Annual Cycle of the Tropical Tropopause Layer with an Idealized Moist Model. *Journal of Climate*, **30 (18)**, 7339–7358, https://doi.org/10.1175/JCLI-D-17-0127.1, URL http://journals.ametsoc.org/doi/10.1175/JCLI-D-17-0127.1.

Kinnison, D. E., and Coauthors, 2007: Sensitivity of chemical tracers to meteorological parameters in the MOZART-3 chemical transport model. *Journal of Geophysical Research*, **112 (D20)**, D20 302, https://doi.org/10.1029/2006JD007879, URL http://doi.wiley.com/10.1029/2006JD007879.

Li, F., and P. Newman, 2020: Stratospheric water vapor feedback and its climate impacts in the coupled atmosphere–ocean Goddard Earth Observing System Chemistry-Climate Model. *Climate Dynamics*, **55 (5-6)**, 1585–1595, https://doi.org/10.1007/s00382-020-05348-6, URL https://link.springer.com/10.1007/s00382-020-05348-6.

Lim, E.-P., H. H. Hendon, and D. W. Thompson, 2018: Seasonal Evolution of Stratosphere-Troposphere Coupling in the Southern Hemisphere and Implications for the Predictability of Surface Climate. *Journal of Geophysical Research: Atmospheres*, **123 (21)**, 002–12, https://doi.org/10.1029/2018JD029321, URL http://doi.wiley.com/10.1029/2018JD029321.

Livesey, N., and Coauthors, 2022: Earth Observing System (EOS). Aura Microwave Limb Sounder (MLS). Version 5.0x Level 2 and 3 data quality and description document. Tech. rep., Jet Propulsion Laboratory, Pasendena, CA, 177 pp. URL https://mls.jpl.nasa.gov/data/datadocs.php.

Manney, G. L., and Coauthors, 2023: Siege in the Southern Stratosphere: Hunga Tonga-Hunga Ha'apai Water Vapor Excluded From the 2022 Antarctic Polar Vortex. *Geophysical Research Letters*, **50 (14)**, https://doi.org/10.1029/2023GL103855.

Marsh, D. R., M. J. Mills, D. E. Kinnison, J.-F. Lamarque, N. Calvo, and L. M. Polvani, 2013: Climate Change from 1850 to 2005 Simulated in CESM1(WACCM). *Journal of Climate*, **26 (19)**, 7372–7391, https://doi.org/10.1175/JCLI-D-12-00558.1, URL http://journals.ametsoc.org/doi/10.1175/JCLI-D-12-00558.1.

Maycock, A. C., M. M. Joshi, K. P. Shine, and A. A. Scaife, 2013: The Circulation Response to Idealized Changes in Stratospheric Water Vapor. *Journal of Climate*, **26 (2)**, 545–561, https://doi.org/10.1175/JCLI-D-12-00155.1, URL http://journals.ametsoc.org/doi/10.1175/JCLI-D-12-00155.1.

Millán, L., and Coauthors, 2022: The Hunga Tonga-Hunga Ha'apai Hydration of the Stratosphere. *Geophysical Research Letters*, **49 (13)**, 1–10, https://doi.org/10.1029/2022GL099381, URL https://onlinelibrary.wiley.com/doi/10.1029/2022GL099381.

Mlawer, E. J., S. J. Taubman, P. D. Brown, M. J. Iacono, and S. A. Clough, 1997: Radiative transfer for inhomogeneous atmospheres: RRTM, a validated correlated-k model for the longwave. *Journal of Geophysical Research*, **102 (D14)**, 16 663, https://doi.org/10.1029/97JD00237, URL http://doi.wiley.com/10.1029/97JD00237.

Neale, R. B., J. Richter, S. Park, P. H. Lauritzen, S. J. Vavrus, P. J. Rasch, and M. Zhang, 2013: The Mean Climate of the Community Atmosphere Model (CAM4) in Forced SST and Fully Coupled Experiments. *Journal of Climate*, **26 (14)**, 5150–5168, https://doi.org/10.1175/JCLI-D-12-00236.1.

Oleson, K. W., D. M. Lawrence, G. B. Bonan, and M. G. Flanner, 2010: Technical Description of version 4.0 of the Community Land Model (CLM). Tech. rep. https://doi.org/10.5065/D6FB50WZ.

Plumb, R. A., 2002: Stratospheric Transport. *J. Meteor. Soc. Japan*, **80 (1949)**, 793–809.

Proud, S. R., A. T. Prata, and S. Schmauß, 2022: The January 2022 eruption of Hunga Tonga-Hunga Ha'apai volcano reached the mesosphere. *Science*, **378 (6619)**, 554–557, https://doi.org/10.1126/science.abo4076, URL https://www.science.org/doi/10.1126/science.abo4076.

Rao, J., C. I. Garfinkel, R. Ren, T. Wu, and Y. Lu, 2023: Southern Hemisphere Response to the Quasi-Biennial Oscillation in the CMIP5/6 Models. *Journal of Climate*, **36 (8)**, 2603–2623, https://doi.org/10.1175/JCLI-D-22-0675.1, URL https://journals.ametsoc.org/view/journals/clim/36/8/JCLI-D-22-0675.1.xml.

Robock, A., 2000: Volcanic eruptions and climate. *Reviews of Geophysics*, **38 (2)**, 191–219, https://doi.org/10.1029/1998RG000054, URL http://doi.wiley.com/10.1029/1998RG000054.

Santer, B. D., and Coauthors, 2014: Volcanic contribution to decadal changes in tropospheric temperature. *Nature Geoscience*, **7 (3)**, 185–189, https://doi.org/10.1038/ngeo2098, URL http://www.nature.com/articles/ngeo2098.

Schoeberl, M. R., Y. Wang, R. Ueyama, A. Dessler, G. Taha, and W. Yu, 2023a: The Estimated Climate Impact of the Hunga Tonga-Hunga Ha'apai Eruption Plume. *Geophysical Research Letters*, **50 (18)**, https://doi.org/10.1029/2023GL104634, URL https://agupubs.onlinelibrary.wiley.com/doi/10.1029/2023GL104634.

Schoeberl, M. R., Y. Wang, R. Ueyama, G. Taha, and W. Yu, 2023b: The Cross Equatorial Transport of the Hunga Tonga-Hunga Ha'apai Eruption Plume. *Geophysical Research Letters*, **50 (4)**, https://doi.org/10.1029/2022GL102443, URL https://agupubs.onlinelibrary.wiley.com/doi/10.1029/2022GL102443.

Sellitto, P., and Coauthors, 2022: The unexpected radiative impact of the Hunga Tonga eruption of 15th January 2022. *Communications Earth & Environment*, **3 (1)**, 288, https://doi.org/10.1038/s43247-022-00618-z, URL https://www.nature.com/articles/s43247-022-00618-z.

Solomon, S., 1999: Stratospheric ozone depletion: A review of concepts and history. *Reviews of Geophysics*, **37 (3)**, 275–316, https://doi.org/10.1029/1999RG900008, URL http://doi.wiley.com/10.1029/1999RG900008.

Solomon, S., K. H. Rosenlof, R. W. Portmann, J. S. Daniel, S. M. Davis, T. J. Sanford, and G. K. Plattner, 2010: Contributions of stratospheric water vapor to decadal changes in the rate of global warming. *Science*, **327 (5970)**, 1219–1223, https://doi.org/10.1126/science.1182488.

Thompson, D. W., M. P. Baldwin, and S. Solomon, 2005: Stratosphere–Troposphere Coupling in the Southern Hemisphere. *Journal of the Atmospheric Sciences*, **62 (3)**, 708–715, https://doi.org/10.1175/JAS-3321.1, URL http://journals.ametsoc.org/doi/abs/10.1175/JAS-3321.1.

Tilmes, S., R. R. Garcia, D. E. Kinnison, A. Gettelman, and P. J. Rasch, 2009: Impact of geoengineered aerosols on the troposphere and stratosphere. *Journal of Geophysical Research*, **114 (D12)**, D12 305, https://doi.org/10.1029/2008JD011420, URL http://doi.wiley.com/10.1029/2008JD011420.

Tritscher, I., and Coauthors, 2021: Polar Stratospheric Clouds: Satellite Observations, Processes, and Role in Ozone Depletion. *Reviews of Geophysics*, **59 (2)**, https://doi.org/10.1029/2020RG000702, URL https://onlinelibrary.wiley.com/doi/10.1029/2020RG000702.

Vernier, J.-P., and Coauthors, 2011: Major influence of tropical volcanic eruptions on the stratospheric aerosol layer during the last decade. *Geophysical Research Letters*, **38 (12)**, L12 807, https://doi.org/10.1029/2011GL047563, URL http://doi.wiley.com/10.1029/2011GL047563.

Vömel, H., S. Evan, and M. Tully, 2022: Water vapor injection into the stratosphere by Hunga Tonga-Hunga Ha'apai. *Science*, **377 (6613)**, 1444–1447, https://doi.org/10.1126/science.abq2299, URL https://www.science.org/doi/10.1126/science.abq2299.

Waters, J., and Coauthors, 2006: The Earth observing system microwave limb sounder (EOS MLS) on the aura Satellite. *IEEE Transactions on Geoscience and Remote Sensing*, **44 (5)**, 1075–1092, https://doi.org/10.1109/TGRS.2006.873771, URL http://ieeexplore.ieee.org/document/1624589/.

Wu, X., S. G. Yeager, C. Deser, N. Rosenbloom, and G. A. Meehl, 2023: Volcanic forcing degrades multiyear-to-decadal prediction skill in the tropical Pacific. *Science Advances*, **9 (15)**, https://doi.org/10.1126/sciadv.add9364, URL https://www.science.org/doi/10.1126/sciadv.add9364.

Zhu, Y., and Coauthors, 2018: Stratospheric Aerosols, Polar Stratospheric Clouds, and Polar Ozone Depletion After the Mount Calbuco Eruption in 2015. *Journal of Geophysical Research: Atmospheres*, **123 (21)**, https://doi.org/10.1029/2018JD028974, URL https://onlinelibrary.wiley.com/doi/10.1029/2018JD028974.

Zhu, Y., and Coauthors, 2022: Perturbations in stratospheric aerosol evolution due to the water-rich plume of the 2022 Hunga-Tonga eruption. *Communications Earth & Environment*, **3 (1)**, 248, https://doi.org/10.1038/s43247-022-00580-w, URL https://www.nature.com/articles/s43247-022-00580-w.

SUPPLEMENTARY

SA. NASA Aura Microwave Limb Sounder (MLS) data

a. Data retrieval

The spatiotemporal evolution of the stratospheric water vapor cloud is examined with data from the Microwave Limb Sounder (MLS) instrument onboard the NASA Aura satellite. Aura was launched in 2004 with a mission to obtain measurements of ozone, aerosol and key gases throughout the atmosphere. The satellite is in a sun-synchronous, near polar orbit at 705 km above the surface with the ascending node in daylight and an equator crossing time at approximately 1345 LT. It constitutes part of NASA's 'A-Train' constellation of satellites.

For this study, daily Version 5 (v5) Level 2 water vapor measurements from MLS are used. For the calculations here, the analysis is focused on the data acquired between 100 hPa and 0.1 hPa pressure levels. Monthly Level 3 data from 2005 through 2021 are also used to compute the climatology. Livesey et al. (2022) provide an assessment of the characteristics and quality of the dataset. All MLS data are acquired from the NASA Earthdata Search web portal at `https://search.earthdata.nasa.gov/search`.

The MLS data users guide (Livesey et al. 2022) outlines screening procedures to be used when examining the water vapor data using the multiple quality control (QC) indicators included in the L2 data files. These include criteria for the precision (> 0), quality (> 0.7), status (even number) and convergence fields (< 2). Additionally, data at pressures > 316 hPa and < 0.0001 hPa should not be used, and values with low values of VMR (< 0.1 ppmv) should be screened out.

In this work, we apply two versions of the QC screening, one with full QC (QC-on) and one where only the pressure and low value screenings are applied (QC-off). The calculated values from these two versions only differ significantly from 15 Jan to 9 Feb 2022. While use of the QC-off fields can introduce uncertainty and is not recommended, it is required to effectively characterize the water vapor plume during the initial weeks following the eruption.

To derive an historical climatology, we process L3 H_2O files with precomputed monthly zonal means from 2005 through 2021. We use monthly data for the climatology to make it smoother than with daily data. Then, this monthly climatology is interpolated to a daily time scale through polynomial interpolation of the monthly values using the built-in IDL function 'spline' with a 'tension' of 0.5. From this procedure, a smooth, physically plausible interpolation is produced.

Several different approaches are used to examine the HTHH water vapor cloud. These are:

- Individual profiles and averages. Native measurements in unitless volume mixing ratio (VMR) versus pressure for individual profiles is examined, as well as averages of these profiles

- Zonal Means. Zonal means are computed with a 4° latitude resolution by averaging all individual VMR profiles in a given latitude bin. This is done at each pressure level. This is consistent with the standard resolution in the Level 3 files.

Two primary calculations are made with the MLS data: 1.) estimates of stratospheric integrated water vapor (SIWV) and 2.) total stratospheric water vapor (TWV) between the 100 hPa and 1 hPa levels and its anomaly. These are calculated as follows:

- Stratospheric integrated water vapor: Water vapor is vertically integrated between 100 and 1 hPa,

$$\mathrm{SIWV} = -\frac{\epsilon}{g}\int_{100hPa}^{1hPa} \mathrm{VMR}\,\mathrm{d}p,$$

  where VMR is the (unitless) volume mixing ratio, p the pressure, g the acceleration due to gravity and $\epsilon = M_{H2O}/M_{air} \approx 0.622$ is the ratio of the molecular weights of water vapor and dry air. Units are converted to $\mathrm{g\,m^{-2}}$, which is equivalent to microns of 'precipitable water'. Typical values range between 2 and 3 $\mathrm{g\,m^{-2}}$. For reference, a uniform increase of 1 ppmv in this calculation is equivalent to an SIWV increase of approximately 0.6 g $\mathrm{m^{-2}}$. This quantity is reported in the zonal mean data and serves as the basis of the total water vapor calculation below.

- Total water vapor and anomaly: Total stratospheric water vapor (TWV) is computed as

$$\mathrm{TWV} = A \cdot \overline{\langle \mathrm{SIWV} \rangle \cos\phi},$$

  where angle brackets represent the zonal mean for SIWV, ϕ is the latitude, the overbar the average and A is the area of the globe between 80°N and 80°S (5.02 x10^{14} $\mathrm{m^2}$). This is multiplied by 10^{-9} to convert into teragrams (Tg) of water vapor. This is done for individual daily zonal means and for the monthly climatological values (that are subsequently interpolated into daily values TWV_C). Using these values, daily anomalies of TWV (TWVA) are estimated as TWVA = TWV - TWV_C.

Using the monthly climatological profiles perturbed by normally distributed errors reflecting the accuracy and precision uncertainties noted by Livesey et al. (2022) with a Monte Carlo approach, the uncertainty estimate in the TWV calculation is ±4 Tg.

b. Determining the vertical profile of HTHH water vapor

The vertical profile of the water vapor anomaly in its initial stages is estimated from the initial overpasses of the HTHH WV cloud. The aim here is to get the relative heights and proportions of mass in the cloud for input into the numerical model.

Three overpasses from 16 January 2022 are examined, with start times of the water vapor cloud encounters at 16/023552 UTC, 16/041445 UTC and 16/150637 UTC, 22 to 36 hours after the eruption with a total of 28 profiles. Millán et al. (2022) confirmed through back-trajectory analysis that these strong H_2O signals originated from HTHH. The vertical profiles from these overpasses are presented in Fig. S1, with the profiles color-coded by overpass. The inset map shows the location of the overpasses relative to the volcano and the geographic features of the region.

These profiles all feature water vapor values higher than the typical background values of 3-5 ppmv. Profiles further west are higher in the atmosphere with green profiles showing two peaks in water vapor VMR at the 0.8 and 4 hPa pressure levels, with peak values of VMR approaching 100 ppmv in the lower peak and 10-20 ppmv in the upper. Red and blue profiles show broad peaks in the lower stratosphere, with peaks at approximately 20 hPa and 30 hPa, respectively. Peak values for both sets of profiles approach 150 ppmv. The red and blue ones are generally rejected by the QC process, producing too large values of 'convergence'. For all three sets of profiles, the average profile is plotted in Fig. S1 as the bold line of the appropriate color. Millán et al. (2022) examined of profiles using v4 of the MLS data and reported values on 16 Jan in that paper that were considerably higher VMRs than shown here, noting that v5 data does a poorer version of retrieving H_2O data in regions of 'extremely enhanced humidity'. This is also consistent with a generally lower values of H_2O retrieved by v5 throughout the atmosphere as noted in the data users guide (Livesey et al. 2022).

Vömel et al. (2022) examined the HTHH H_2O anomaly using radiosonde data, showing strongly enhanced humidity values between 20 and 30 km (approximately 90 to 10 hPa), with values at individual levels approaching 1000 ppmv in some instances. The heights where these anomalies are found in the sonde data agree very well the heights of the water vapor anomaly in the MLS data, although the values of the anomaly are considerably lower in MLS. This latter observation is not surprising, given the differences in sampling between the measurements; MLS represents a vertically and horizontally smoothed observations while radiosondes are high resolution, nearly 'instantaneous' values. This favorable comparison with independent observations supports the idea that these signals in the MLS are genuine, despite not passing the QC and that they are suitable to use in further analysis.

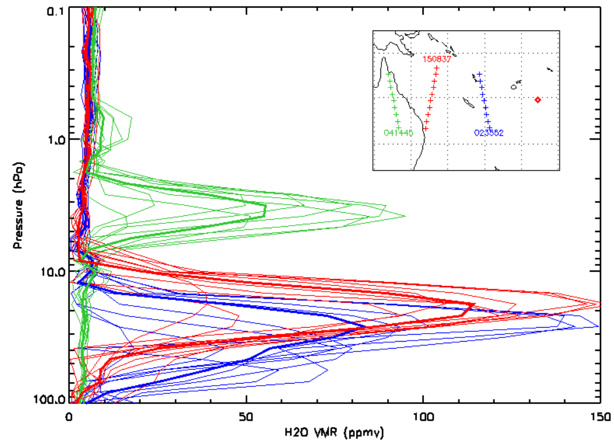

Fig. S1. Vertical Profiles of water vapor from three MLS overpasses. See text for details.

Using the average profiles from each of the three overpasses, the mean vertical profile of H_2O from the HTHH eruption can be determined. This is done by merging the three mean profiles; above 10 hPa, the mean of the green profiles is used; below 10 hPa, an average of the mean red and blue profiles is used. From this profile, the SIWV is computed over each set of 3 non-overlapping levels and divided by the total SIWV over all levels to obtain a fraction of total mass with height, yielding a scalable profile of the vertical distribution of H_2O mass in the eruption. This is shown in Fig. 1b. Two primary injection heights are identified in the profile, one near 25 hPa and the other near 4 hPa. A smaller third is also found near 0.8 hPa but contains only a small fraction of the mass. Approximately 94% of the total mass is injected below 10 hPa, generally at heights between 22 and 27 km. Most of the remaining 6% of the mass above 10 hPa is found between approximately 36 and 38 km altitude.

c. Temporal evolution of total water vapor

Fig. S2 shows the evolution of TWV between 26 Nov 2021 and 17 Nov 2023. This includes the time before the first eruption of HTHH on 19 December 2021 and the initial residence time of the H_2O cloud in the stratosphere. Time series for both QC-on and QC-off realizations are shown, along with the MLS-based climatology. Prior to 15 January 2022 and after 9 February 2022, the two series are effectively identical; as noted by Millán et al. (2022) the difference lies in the application of the QC during the initial weeks of the eruption. The QC-off realization displays a sharp discontinuity at the time of the 3rd eruption, although still does not reach its highest value until 2 weeks past the eruption. The QC-on curve shows a much more gradual increase after the eruption that is physically inconsistent with the idea of a short, sharp eruption. RMS

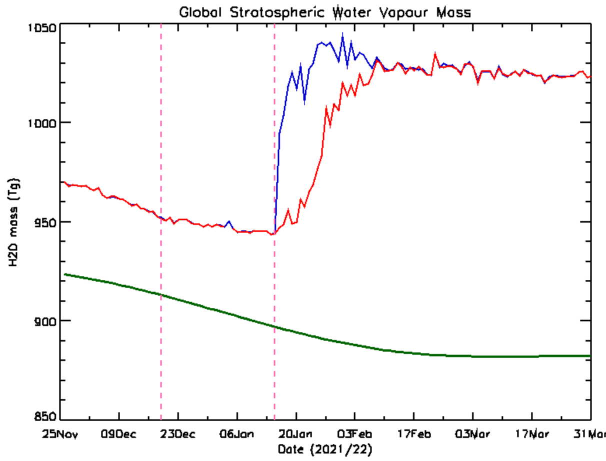

FIG. S2. Time series of QC-off (blue) and QC-on (red) time series of v5 MLS H_2O, v5 2005-2021 climatology shown as green line. Times of eruption 1 (19 Dec 21) and eruption 3 (15 Jan 2022) highlighted.

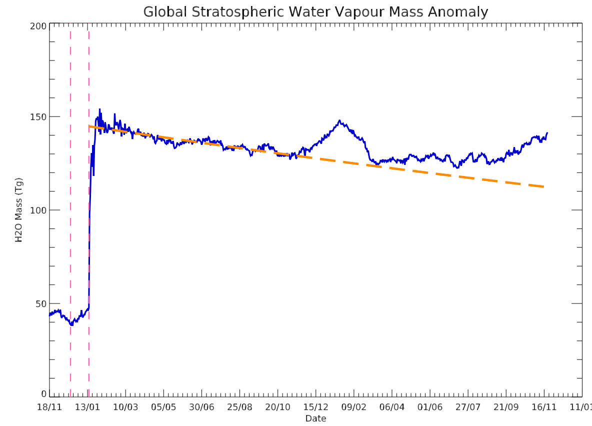

FIG. S3. Time series of anomalous global stratospheric water vapor. Orange dash line represents the exponential fit. See text for details.

uncertainty in the calculation of TWV is approximately ±4 Tg, corresponding to random errors of approximately 10%.

Other features of note in Fig. S2 are:

- The substantial pre-existing anomaly in TWV of 40-50 Tg that was present prior to the eruption. Analysis of earlier data (not shown) indicates that anomalies were near zero in early June 2019 and began to rise more sharply in January 2020 and have slowly increased since that time.

- An inflection point in the TWV time series that is coincident with the first eruption of HTHH on 19 Dec 2021. Rather than a distinct increase in TWV, a subtle shift in the rate of decline is noted, from more quickly than climatology before to slower afterwards. This is perhaps suggestive of a very small water vapor emission from the first eruption or another (unknown) change in the sink of stratospheric water vapor at that time.

d. Evolution of anomalies and estimated HTHH H_2O emission

Fig. S3 depicts the TWV anomaly for the period from 25 November 2021 until 17 November 2023 using the QC-off realization data. As before, the sharp discontinuity at the time of the eruption is readily apparent; peak value of the anomaly is 150 Tg approximately two weeks after the eruption. The anomaly field is particularly noisy around the time of the peak. Also apparent are the pre-existing anomaly and the inflection point coincident with the first eruption. In the 5 days before the eruption, the average anomaly is 46.8 Tg.

Because of potential errors introduced by the QC-off processing and the slow evolution of peak anomalies, it is difficult to directly estimate the anomaly associated with HTHH. This is addressed here through curve fitting and extrapolation. The water vapor anomaly is assumed to decay exponentially following $A = A_0 e^{rt}$, where A_0 is the initial anomaly, r is the rate of change constant, presumably negative, and t is the time in days. The rate of change constant is estimated by calculating the regression coefficient of the logarithm of the anomaly data from 10 Feb-1 Oct 2022, the period over which the QC-on and QC-off data are equivalent. The best estimate is r=-3.87x10^{-4} ± 3.33x10^{-5} day^{-1}(2-s uncertainty), a decay rate of approximately -1.13% per month. The initial value is then determined by calculating the estimated A_0 value from all the data in the regression and taking the mean. The provides an estimate of A_0 =144.8 ± 2.0 Tg (1-sd uncertainty); estimates range from 139.5 to 153.9 Tg. There is some sensitivity to the choice of end time, and cutting off the data in May or June gives slightly higher estimates of both variables (e.g. A_0 ~148 Tg, r = -2.1% month) but results in a significantly worse fit for the later data. Note that the slightly different values of r reported here compared to those given in the main text arise from a fit of daily data here versus monthly data in the main text.

Using these numbers, we can estimate the total H_2O anomaly from HTHH eruption as 144.6 – 46.8 = 97.8 ± 6 Tg, approximately 11% of the TWV for the season as computed here. This estimate lies in the middle of the radiosonde estimates of Vömel et al. (2022) (i.e. 'at least' 50 Tg reported) and the MLS estimates by Millán et al. (2022) (i.e. 146 Tg). We note that without considering the pre-existing anomaly, our estimate of matches quite closely with the latter result, as might be expected. It is not clear from the text if that was considered in their result. Alternately, the differences could be the result of using v5 versus v4 of the MLS data.

From this estimate of A_0 and the model of exponential decay, it is noted that estimates of H_2O anomaly directly from MLS remain biased quite low despite the use of QC-off data. For example, on 16 January, the observed anomaly value is 98.3 Tg, for an HTHH anomaly estimate of 51.5 Tg, approximately half of the 'true' estimate. This bias has at least two sources:

- The previously mentioned v4 vs v5 differences, in particular those relating to the 'pointing error' (Millán et al. 2022). The earlier version of the algorithm simply performs better in high humidity situations than the current version.
- The TWV methodology here is reliant on the zonal mean calculation which is strongly impacted by the highly skewed zonal distribution of H_2O before the global dispersion of the H_2O cloud. In the first few days in particular, H_2O is concentrated in a small area of the globe, while the rest has near-climatological values. This has the effect of underestimating the zonal mean, which feeds into the TWV calculation and results in an underestimate of that value.

e. Anomaly Lifetime

The lifetime of the HTHH anomaly can be estimated using the model of exponential decay. Using the estimated value of r (-3.87 x10^{-4} day^{-1}), the estimated time to decay back to the initial anomaly of 46.8 Tg is 2919 days; for ±2s, the values range from 2681-3186 days. Translating to years, the range is about 7-9 years, meaning that the water vapor anomaly should no longer be elevated (above its 10-14 January 2022 value) at some point during 2029 or 2030. This calculation assumes that the rate from mid-February to early-October is the correct one and that no other sinks or sources of stratospheric H_2O occur. As noted earlier, sensitivity to the choice of endpoints is important.

SB. Additional figures

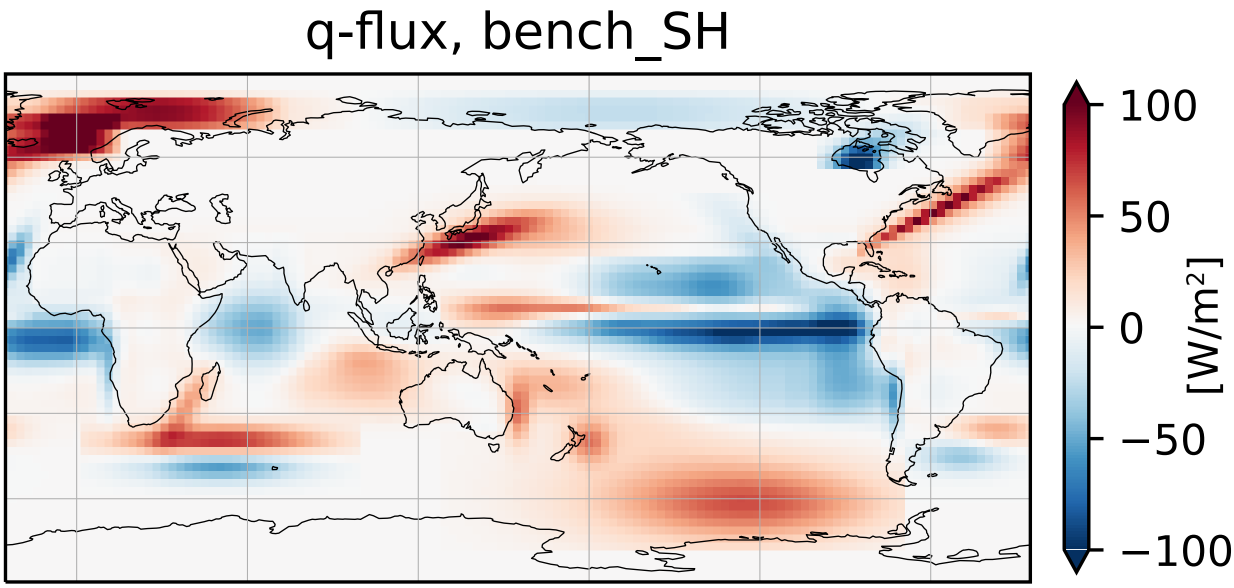

Fig. S4. Ocean surface heat fluxes [W/m^2] for MiMA, which includes the major ocean currents plus a realistic ITCZ and SPCZ.

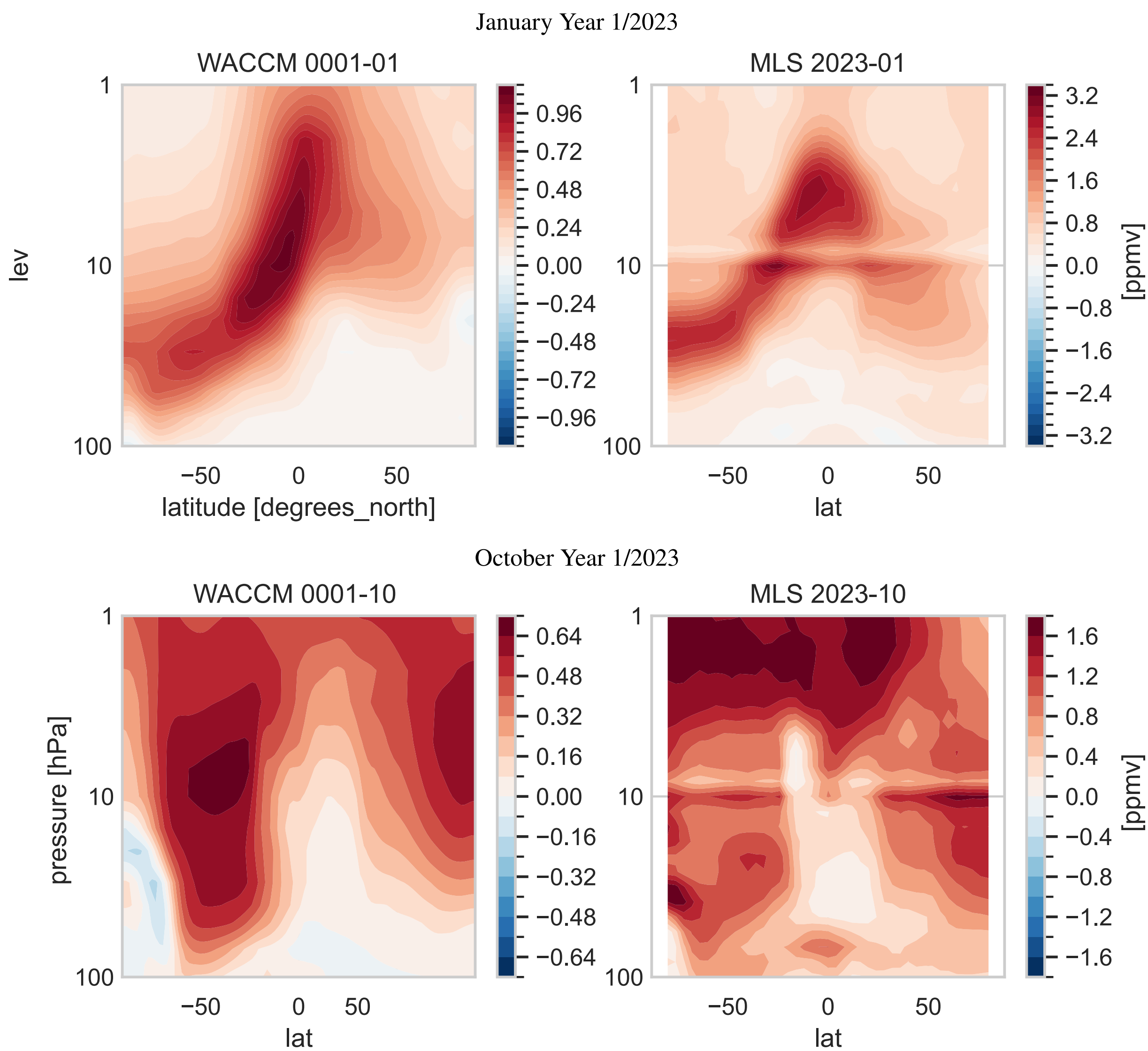

Fig. S5. Stratospheric water vapor (SWV) anomalies in (left) WACCM and (right) MLS for (top) January and (bottom) October of year 1/2023. While model and observations agree in the general structure and evolution of the SWV anomalies due to HTHH, there is a positive anomaly in the tropical tropopause layer in MLS (100-70hPa, right panels) which we attribute to tropical convective activity rather than the HTHH eruption. Note the difference in color scales between WACCM and MLS plots.

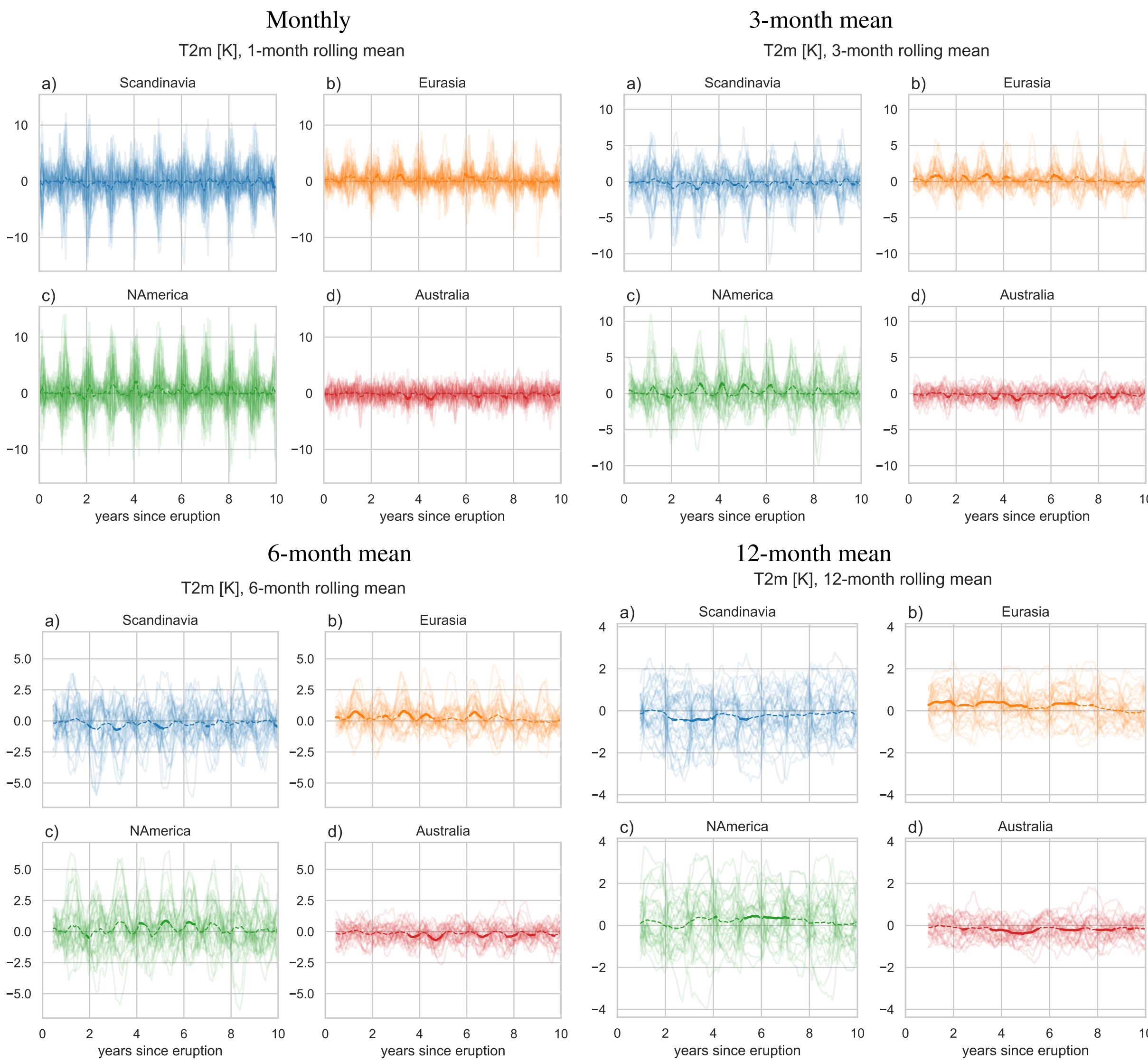

Fig. S6. Spaghetti plots of regional rolling means of surface temperature anomalies over (blue) Scandinavia, (orange) Eurasia, (green) North America, and (red) Australia from Figs. 7 and 8. Shown are all members, and the ensemble means with a thick line. A continuous thick line means the ensemble mean is significantly different from zero. Rolling means are over (top left) 1 month, (top right) 3 months, (bottom left) 6 months, and (bottom right) 12 months.

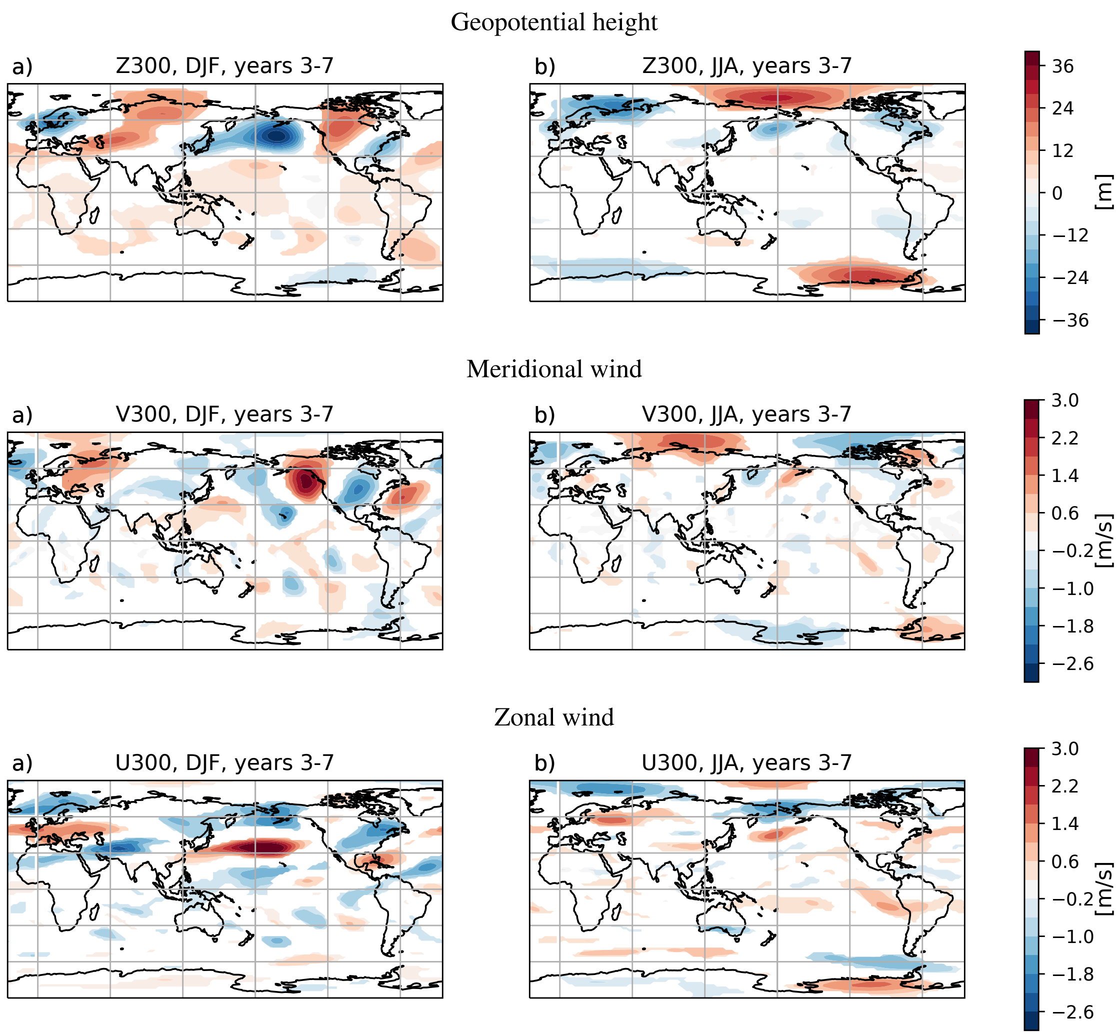

FIG. S7. Year 3-7 seasonal means of 300hPa (top) geopotential height [m], (middle) meridional wind [m/s], and (bottom) zonal wind [m/s] anomalies. All variables confirm the wave structure discussed in Fig. 10.

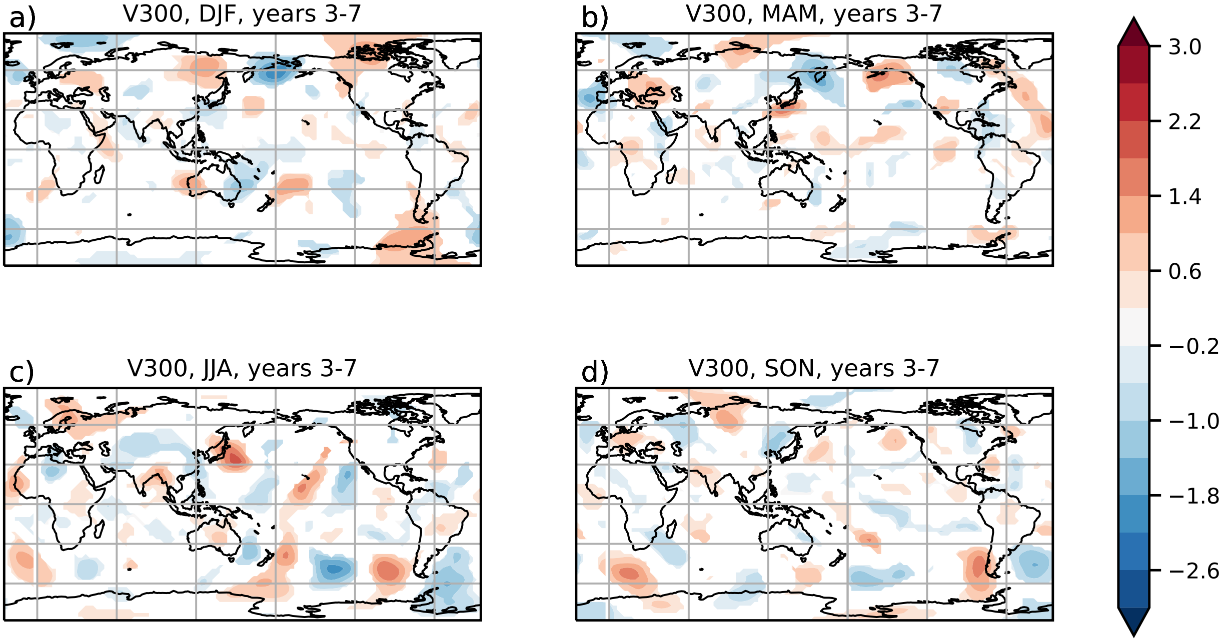

Fig. S8. Meridional wind anomalies [m/s] similar to Fig. S7(middle), but for MiMA simulations.

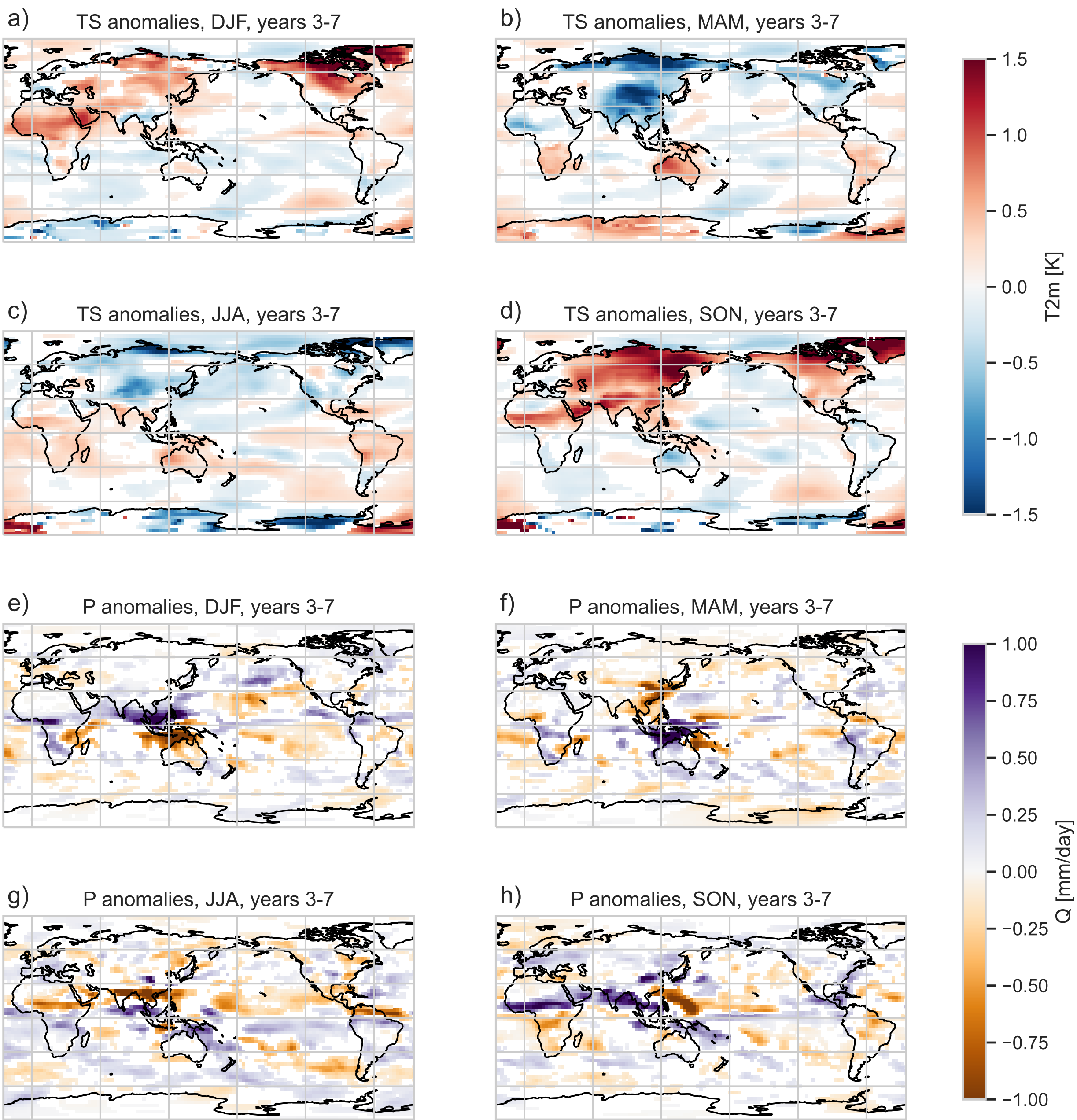

Fig. S9. MiMA simulations similar to those discussed in Fig. 11, but with WACCM anomalies of SWV only.

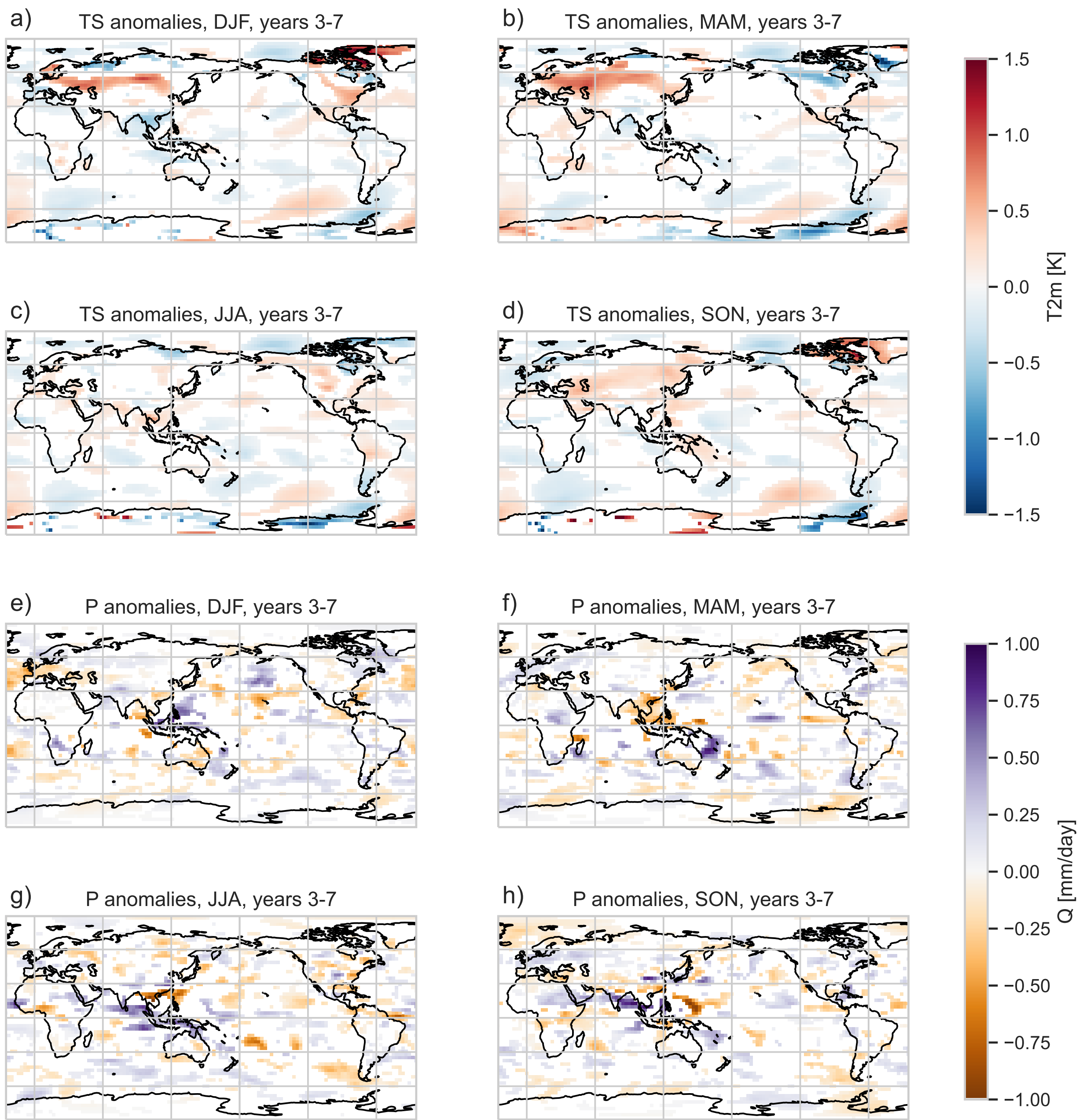

FIG. S10. MiMA simulations similar to those discussed in Fig. 11, but with WACCM anomalies of ozone only.

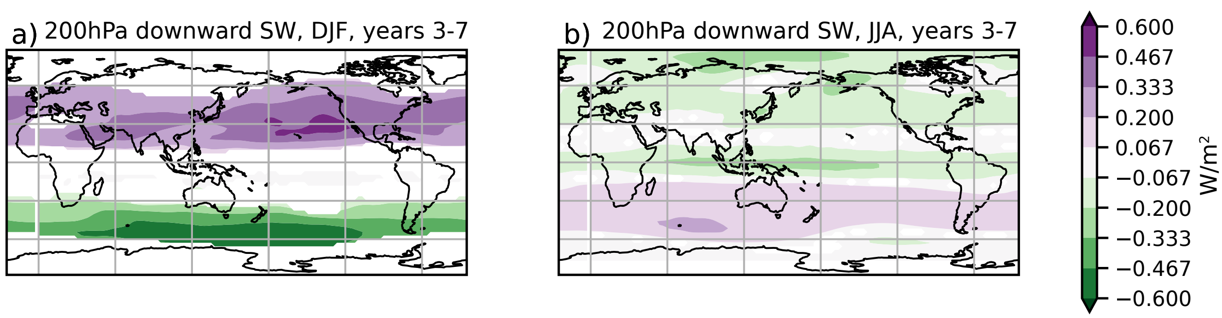

Fig. S11. 200hPa downward shortwave flux anomalies from MiMA. Purple shading indicates less absorption in the stratosphere, green shading more absorption.